

SDSS IV MaNGA - Metallicity and ionisation parameter in local star-forming galaxies from Bayesian fitting to photoionisation models

M. Mingozi^{1,2,3}, F. Belfiore^{2,4}, G. Cresci², K. Bundy⁵, M. Bershadsky^{6,7}, D. Bizyaev^{8,9}, G. Blanc^{10,11}, M. Boquien¹², N. Drory¹³, H. Fu¹⁴, R. Maiolino^{15,16}, R. Riffel^{17,18}, A. Schaefer⁶, T. Storchi-Bergmann^{17,18}, E. Telles¹⁹, C. Tremonti⁶, N. Zakamska²⁰, and K. Zhang²¹

¹ Dipartimento di Fisica e Astronomia, Università degli Studi di Bologna, Via Piero Gobetti 93/2, I-40129, Bologna, Italy
e-mail: matilde.mingozzi@inaf.it

² INAF – Osservatorio Astrofisico di Arcetri, Largo E. Fermi 5, I-50157, Firenze, Italy

³ INAF – Osservatorio Astrofisico di Padova, Vicolo dell’Osservatorio 5, I-35122, Padova, Italy

⁴ European Southern Observatory, Karl-Schwarzschild-Str. 2, Garching bei München, D-85748, Germany.

⁵ University of California Observatories, University of California Santa Cruz, 1156 High St., Santa Cruz, CA 95064, USA

⁶ Department of Astronomy, University of Wisconsin-Madison, 475N. Charter St., Madison, WI 53703, USA

⁷ South African Astronomical Observatory, P.O. Box 9, Observatory 7935, Cape Town, South Africa

⁸ Apache Point Observatory and New Mexico State University, Sunspot, NM, 88349, USA

⁹ Sternberg Astronomical Institute, Moscow State University, Moscow, Russia

¹⁰ Observatories of the Carnegie Institution for Science, 813 Santa Barbara St., Pasadena, CA, USA

¹¹ Departamento de Astronomía, Universidad de Chile, Camino del Observatorio 1515, Las Condes, Santiago, Chile

¹² Centro de Astronomía (CITEVA), Universidad de Antofagasta, Avenida Angamos 601, Antofagasta, Chile

¹³ McDonald Observatory, The University of Texas at Austin, 1 University Station, Austin, TX 78712, USA

¹⁴ Department of Physics & Astronomy, The University of Iowa, 203 Van Allen Hall, Iowa City, IA 52242, USA

¹⁵ Cavendish Laboratory, University of Cambridge, 19 J. J. Thomson Avenue, Cambridge CB3 0HE, UK

¹⁶ Kavli Institute for Cosmology, University of Cambridge, Madingley Road, Cambridge CB3 0HA, UK

¹⁷ Laboratório Interinstitucional de e-Astronomia - LIneA, Rua General José Cristino 77, Rio de Janeiro, RJ 20921-400, Brazil

¹⁸ Universidade Federal do Rio Grande do Sul, IF, CP 15051, Porto Alegre 91501-970, RS, Brazil

¹⁹ Observatório Nacional, Rua José Cristino, 77, Rio de Janeiro, RJ, 20921-400, Brasil

²⁰ Center for Astrophysical Sciences, Department of Physics and Astronomy, Johns Hopkins University, 3400 North Charles Street, Baltimore, MD 21218, USA

²¹ Lawrence Berkeley National Laboratory, 1 Cyclotron Road, Berkeley, CA 94720, USA

Received XXX; accepted XXX

ABSTRACT

We measured gas-phase metallicity, ionisation parameter and dust extinction for a representative sample of 1795 local star-forming galaxies using integral field spectroscopy from the SDSS-IV MaNGA survey. We self-consistently derive these quantities by comparing observed line fluxes with photoionisation models using a Bayesian framework. We also present the first comprehensive study of the $[S\text{ III}]\lambda\lambda 9069, 9532$ nebular lines, which have long been predicted to be ideal tracers of the ionisation parameter. Unfortunately, we find that current photoionisation model predictions substantially over-predict the intensity of the $[S\text{ III}]$ lines, while broadly reproducing other observed optical line ratios. We discuss how to nonetheless make use of the information provided by the $[S\text{ III}]$ lines by setting a prior on the ionisation parameter. Following this approach, we derive spatially-resolved maps and radial profiles of metallicity and ionisation parameter. The metallicity radial profiles derived are comparable with previous works, with metallicity declining toward the outer parts and a flattening in the central regions, in agreement with infall models of galaxy formation, that predict that spiral discs build up through accretion of material, which leads to an inside-out growth. On the other hand, ionisation parameter radial profiles are flat for low-mass galaxies, while their slope becomes positive as galaxy mass increases. However, the ionisation parameter maps we obtain are clumpy, especially for low-mass galaxies. The ionisation parameter is tightly correlated with the equivalent width of $H\alpha$ $[EW(H\alpha)]$, following a nearly universal relation, which we attribute to the change of the spectral shape of ionising sources due to ageing of $H\text{ II}$ regions. We derive a positive correlation between ionisation parameter and metallicity at fixed $EW(H\alpha)$, in disagreement with previous theoretical work expecting an anti-correlation.

Key words. Galaxies: ISM – Galaxies: abundances – Galaxies: evolution

1. Introduction

The metal content in galaxies is mainly governed by the interplay of inflows of gas and metals from the circum- and intergalactic medium, metal production via stellar nucleosynthesis and out-

flows via galactic winds. Because of these connections, the abundance and distribution of metals in the interstellar medium (ISM) of local galaxies provides strong constraints on current models of galaxy evolution (e.g. Lilly et al. 2013; Maiolino & Mannucci 2019).

Emission lines, originating from nebulae photoionised by massive stars, represent one of the most powerful tracers of the metal abundance in both nearby galaxies and the high-redshift Universe. Gas-phase metallicity is commonly traced by the abundance of oxygen, because of its high relative abundance and the availability of lines of the dominant ionic species in the optical wavelength range. Moreover, the production of oxygen is less complex compared to other elements such as nitrogen and carbon. Therefore, in this paper we use metallicity and oxygen abundance ($12+\log(\text{O}/\text{H})$) interchangeably, as commonly done in studies of chemical abundances based on H II regions. In particular, measurement of the [O III] $\lambda\lambda 4363$ auroral line together with the [O III] $\lambda\lambda 4959, 5007$ nebular lines allows the determination of the electron temperature of the H II region. When combined with other temperature-sensitive lines the ionisation structure of the nebula and metal content can be derived with a set of minimal assumptions (e.g. Stasińska 2004). Auroral lines, however, are often too weak to be detected in extragalactic sources at even modest redshifts and in large galaxy surveys (e.g. Stasińska 2005), and thus this method is still mostly limited to a low number of galaxies and often biased towards luminous and metal-poor regions (e.g. Andrews & Martini 2013; Jones et al. 2015; Sanders et al. 2016; Yates et al. 2019).

In light of this, Pagel et al. (1979) and Alloin et al. (1979) suggested methods to estimate the metallicity of H II regions using strong emission lines (SEL) only. Traditionally, this approach relies on the choice of a metallicity *diagnostic* (i.e. one or several line ratios) combined with an abundance calibration prescription. Among the most widely used metallicity diagnostics there are $R23 = ([\text{O III}]\lambda\lambda 4959, 5007 + [\text{O II}]\lambda\lambda 3726, 29)/\text{H}\beta$ (Pagel et al. 1979; Pilyugin & Thuan 2005), $\text{O3N2} = ([\text{O III}]\lambda\lambda 4959, 5007/\text{H}\beta)/([\text{N II}]\lambda\lambda 6548, 84/\text{H}\alpha)$ (Pettini & Pagel 2004; Marino et al. 2013; Curti et al. 2017) and $\text{N2} = [\text{N II}]\lambda\lambda 6548, 84/\text{H}\alpha$ (Storchi-Bergmann et al. 1994; Denicoló et al. 2002), together with other combinations of multiple line ratios (e.g. Pilyugin & Mattsson 2011; Pilyugin et al. 2012). Each diagnostic has advantages and drawbacks, making it suitable in different situations. Nevertheless, different metallicity calibrations, even when based on the same diagnostic, are generally not mutually consistent leading to e.g. offsets of 0.2-0.6 dex in the absolute abundance scale (Kewley & Ellison 2008; Blanc et al. 2015). The origins of this discrepancy are still largely debated in the literature.

An important limitation of the “strong-line approach” to determining metallicity is the secondary dependence of metallicity diagnostics on other parameters of the ISM, such as the ionisation parameter (q), as well as relative chemical abundances and the shape of the ionising continuum. The ionisation parameter is defined as the ratio of the number flux of ionising photons to the density of hydrogen atoms. In a spherical geometry it can be defined as

$$q = \frac{Q_{ion}}{4\pi r^2 n_e}, \quad (1)$$

where Q_{ion} is the number of ionising photons emitted per unit time, r is the distance between the source and the emitting cloud, and n_e is the electron density.

In this work we move past the traditional SEL diagnostics of metallicity and instead make use of a Bayesian approach, based on Blanc et al. (2015), and inspired by the previous work of Charlot & Longhetti (2001), Brinchmann et al. (2004) and Tremonti et al. (2004). In this framework, observed SEL fluxes are directly compared with a grid of photoionisation models. This approach has the advantage of modelling all the available

SEL ratios self-consistently, but is also subject to specific limitations. First, the current generation of photoionisation models are not capable of correctly reproducing all the observable SEL ratios (D’Agostino et al. 2019). Second, photoionisation models are based on a large number of simplifying assumptions and it is not guaranteed that the obtained solution is unique and that the real uncertainties are correctly estimated. Moreover, any physical correlation between metallicity and ionisation parameter, which is hard-wired into empirical models, cannot be easily ported to Bayesian methods. When using a Bayesian approach it is therefore necessary to use a wide enough set of SELs to break the well-known degeneracy between metallicity and q .

Empirically the ionisation parameter is best determined by ratios of emission lines of different ionisation stages of the same element, with $\text{O3O2} = [\text{O III}]\lambda\lambda 4959, 5007/[\text{O II}]\lambda\lambda 3726, 29$ being the most widely used proxy in the optical wavelength range (Díaz & Pérez-Montero 2000; Kewley & Dopita 2002; Kobulnicky & Kewley 2004). O3O2 , however, is strongly dependent on metallicity, as shown for example in Kewley & Dopita (2002), since the [O II] lines can only be excited by relatively high temperatures, and thus disappear in cooler, high-metallicity H II regions. Kewley & Dopita (2002) demonstrated that the ratio between S^{++} and S^+ , traced by $[\text{S III}]\lambda\lambda 9069, 9532/[\text{S II}]\lambda\lambda 6717, 32$ (S3S2), provides a more accurate measure of the ionisation parameter, as already suggested by Mathis (1982, 1985); Dopita & Evans (1986). Given the redder wavelengths of the sulphur emission lines, and consequently their lower excitation energies with respect to the oxygen lines, S3S2 is roughly independent of metallicity (e.g. variation of 0.3 dex in the range of $7.63 < \log(\text{O}/\text{H}) + 12 < 8.93$, Kewley et al. 2019). Furthermore, Kewley et al. (2019) argued that S3S2 is also insensitive to ISM pressure P for $4 < \log(P/k) < 7$.

Until recently, however, the near-infrared $[\text{S III}]\lambda\lambda 9069, 9532$ lines (from now on referred to as the [S III] lines), have only rarely been used to investigate the ionisation parameter (see work by Díaz & Pérez-Montero 2000; Kehrig et al. 2006) because they are weaker than their oxygen counterparts and no large spectroscopic survey of nearby galaxies covered the required wavelength range. This situation is now changing, with more facilities covering the full wavelength range between 6000 and 10000 Å, including the X-shooter and MUSE instruments on the VLT (Cresci et al. 2017; Mingozzi et al. 2019; Kreckel et al. 2019), MODS on LBT, or the SDSS-IV MaNGA survey and the first detection of the [S III] lines at high redshift with near-IR instruments (e.g. Curti et al. 2019a; Sanders et al. 2019).

In this paper, we make use of data from the MaNGA survey (Bundy et al. 2015; Yan et al. 2016), part of the last generation Sloan Digital Sky Survey IV (SDSS IV, July 2014–2020), to study metallicity and ionisation parameter of local galaxies in a Bayesian framework. Specifically, we present the first study of the [S III] lines, and therefore a detailed characterisation of the ionisation parameter, in a large sample of local galaxies. Based on our improved measurements of the ionisation parameter, we aim to characterise how q varies within galaxies, across different stellar masses, and investigate what relation (if any) exists between ionisation parameter and other key physical parameters of the H II regions, such as metallicity, star formation rate surface density and age.

The paper is structured as follows. In Sec. 2 we introduce the galaxy sample and the data analysis, while in Sec. 3 we discuss the Bayesian method we employ to derive metallicity, ionisation parameter and gas extinction, highlighting the fundamental role played by [S III] lines. In Sec. 4 we present and discuss our

results, while in Sec. 5 we conclude, highlighting benefits and drawbacks of our approach.

Throughout this work, we use a Λ cold dark matter cosmology with $\Omega_M = 0.3$, $\Omega_\Lambda = 0.7$ and $H_0 = 70 \text{ km}^{-1} \text{ s}^{-1} \text{ Mpc}^{-1}$.

2. Data and sample

2.1. The galaxy sample

The MaNGA survey is one of the three components of SDSS-IV (Blanton et al. 2017). Observations are carried out at the 2.5 m telescope at Apache Point Observatory (Gunn et al. 2006). The survey aims to map 10000 galaxies in the redshift range $0.01 < z < 0.15$ by 2020. MaNGA galaxies are selected to be representative of the overall galaxy population for $\log(M_\star/M_\odot) > 9$. The sample is drawn from an extended version of the NASA-Sloan catalogue (NSA v1_0_1¹, Blanton et al. 2011). MaNGA observations are carried out with 17 hexagonal fiber-bundle integral field units (IFUs) that vary in diameter from 12" (19 fibers) to 32" (127 fibers). Each fiber has a diameter of 2" (Drory et al. 2015). The IFUs feed light into the two dual-channel BOSS spectrographs, that provide simultaneous wavelength coverage in the 3600–10300 Å wavelength range, with a resulting spectral resolution of $R \sim 1400$ at $\lambda \sim 4000 \text{ Å}$ and $R \sim 2600$ near $\lambda \sim 9000 \text{ Å}$ ($R \sim 2000$ corresponds to a velocity dispersion of $\sigma \sim 70 \text{ km/s}$, Smee et al. 2013). A uniform radial coverage to radii of $1.5 R_e$ and $2.5 R_e$ is achieved for 2/3 (primary sample) and 1/3 (secondary sample) of the final sample, respectively. In order to compensate for light loss during observations, a three-point dithering pattern is used, allowing also to obtain a uniform point spread function (PSF, Law et al. 2015).

The data analysed in this paper are part of the fifteenth SDSS Data Release (DR15, Aguado et al. 2019), reduced according to the algorithms described in Law et al. (2016) and Yan et al. (2016) and subsequent updates. The data release includes the output of the MaNGA data analysis pipeline (DAP, Westfall et al. 2019; Belfiore et al. 2019) for a sample of 4688 spatially-resolved galaxies observed until July 2017. Integrated galaxy global properties such as redshift, total stellar mass (M_\star), elliptical effective radius (R_e) and inclinations are drawn from the extended version of NSA v1_0_1, i.e. the parent targeting catalog described in Section 2 of Wake et al. (2017), which includes the calculation of elliptical Petrosian aperture photometry. Elliptical Petrosian effective radii and inclinations are used throughout this work to construct de-projected radial gradients.

From this initial sample of galaxies, we selected 4099 objects with $z < 0.08$, in order to have access to the $[\text{S III}]\lambda 9532$ line within the observed wavelength range. We select star-forming galaxies according to the ‘excitation morphology’, as described in Belfiore et al. (2016). This scheme makes use of the classical Baldwin-Phillips-Terlevich (BPT) diagnostic diagram (Baldwin et al. 1981; Veilleux & Osterbrock 1987; Kauffmann et al. 2003; Kewley et al. 2006) to map the excitation source of the ISM throughout galaxies. In particular, we exclude galaxies that show central or extended low-ionisation emission-line regions (cLIERs and eLIERs), line-less galaxies (no line emission detected), and galaxies with Seyfert-like central regions. We retain only objects classified as star-forming, defined as objects dominated by star formation (SF) at all radii. This selection cut limits our sample to mostly main-sequence galaxies, while eliminating the majority of green valley objects (Belfiore et al. 2018) and all

passive galaxies. Finally, we exclude highly inclined systems, namely galaxies with minor to major axis ratio (b/a) less than than 0.4, leading to a final sample of 1795 galaxies.

In the rest of this work we further exclude spaxels which are not classified as star-forming according to either the $[\text{N II}]$ - or the $[\text{S II}]$ -BPT diagrams (i.e. all the spaxels above the demarcation lines defined by Kauffmann et al. 2003 and by Kewley et al. 2001, respectively), for which we assume that the $\text{H}\alpha$ flux is contaminated by other physical processes aside from star formation.

2.2. Spectral fitting

We make use of the flux measurements obtained by Gaussian fitting for the $[\text{O II}]\lambda\lambda 3726, 29$, $\text{H}\beta$, $[\text{O III}]\lambda\lambda 4959, 5007$, $[\text{N II}]\lambda\lambda 6548, 84$, $\text{H}\alpha$, $[\text{S II}]\lambda 6717$ and $[\text{S II}]\lambda 6731$ emission lines in stellar-continuum subtracted spectra from the MaNGA DAP v2.2.1. In the fit performed by the DAP the flux ratios of doublets are fixed when such ratios are determined by atomic physics, with transition probabilities taken from Osterbrock & Ferland (2006) (e.g. intrinsic ratios of 0.340 and 0.327 for $[\text{O III}]$ and $[\text{N II}]$ doublets, respectively). Furthermore, in DR15 the velocities of all the fitted emission lines are tied, while the velocity dispersions are free to vary, with the exception of the doublets with fixed flux ratios and the $[\text{O II}]\lambda\lambda 3726, 29$ lines. Belfiore et al. (2019) (see Sec. 2.2.3) found that the impact of these algorithmic choices on the line fluxes is negligible.

In DR15, the stellar continuum fitting is limited by the spectral range of the adopted MILES stellar library (Sánchez-Blázquez et al. 2006; Falcón-Barroso et al. 2011). Because of the absence of a continuum model redder than $\sim 7400 \text{ Å}$ the DAP does not fit the $[\text{S III}]\lambda\lambda 9069, 9532$ lines. We therefore performed a bespoke fitting process.

Since the red part of the spectrum around the lines of interest does not feature prominent stellar absorption features, we use a linear baseline to account for the local continuum $\pm 30 \text{ Å}$ around the $[\text{S III}]$ emission lines. Each line is then fitted with a single Gaussian, making use of MPFIT (Markwardt 2009) and masking the remaining part of the spectrum. We fixed the flux ratio of the two $[\text{S III}]$ lines to the theoretical ratio of 2.47 determined from the transition probabilities used in PYNEB (Luridiana et al. 2015) and their velocities to the velocity obtained by the DAP for the previously fitted emission lines. Lower ($\sim 40 \text{ km/s}$) and upper ($\sim 400 \text{ km/s}$) limits are imposed on the velocity dispersion in order to reduce the probability of fitting sky lines, or noise features in the spectra. All line fluxes are corrected for Galactic foreground extinction using the maps of Schlegel et al. (1998) and the reddening law of O’Donnell (1994).

The top panel of Fig. 1 shows the g-r-i image composite from SDSS of MaNGA galaxy 8150-6103 with the MaNGA hexagonal field of view (FoV) overlaid (on the left), and an example of our fitting procedure for the $[\text{S III}]$ lines for one spaxel (on the right). The observed spectrum is reported in black, while the best-fit is highlighted by the dashed-dotted red line. The regions in grey were masked before fitting. The bottom panel of Fig. 1 presents maps of the $[\text{S III}]\lambda 9532$ flux, velocity and velocity dispersion for the same galaxy.

In Appendix A, we present a comparison between the emission line fluxes considered in this work and those computed by the Pipe3D code (Sánchez et al. 2016, 2018), which performs independent continuum subtraction and emission-line measurements of the MaNGA data. There is a good overall agreement between the two (see also the Appendix of Belfiore et al. 2019),

¹ <https://www.sdss.org/dr15/manga/manga-target-selection/nsa/>

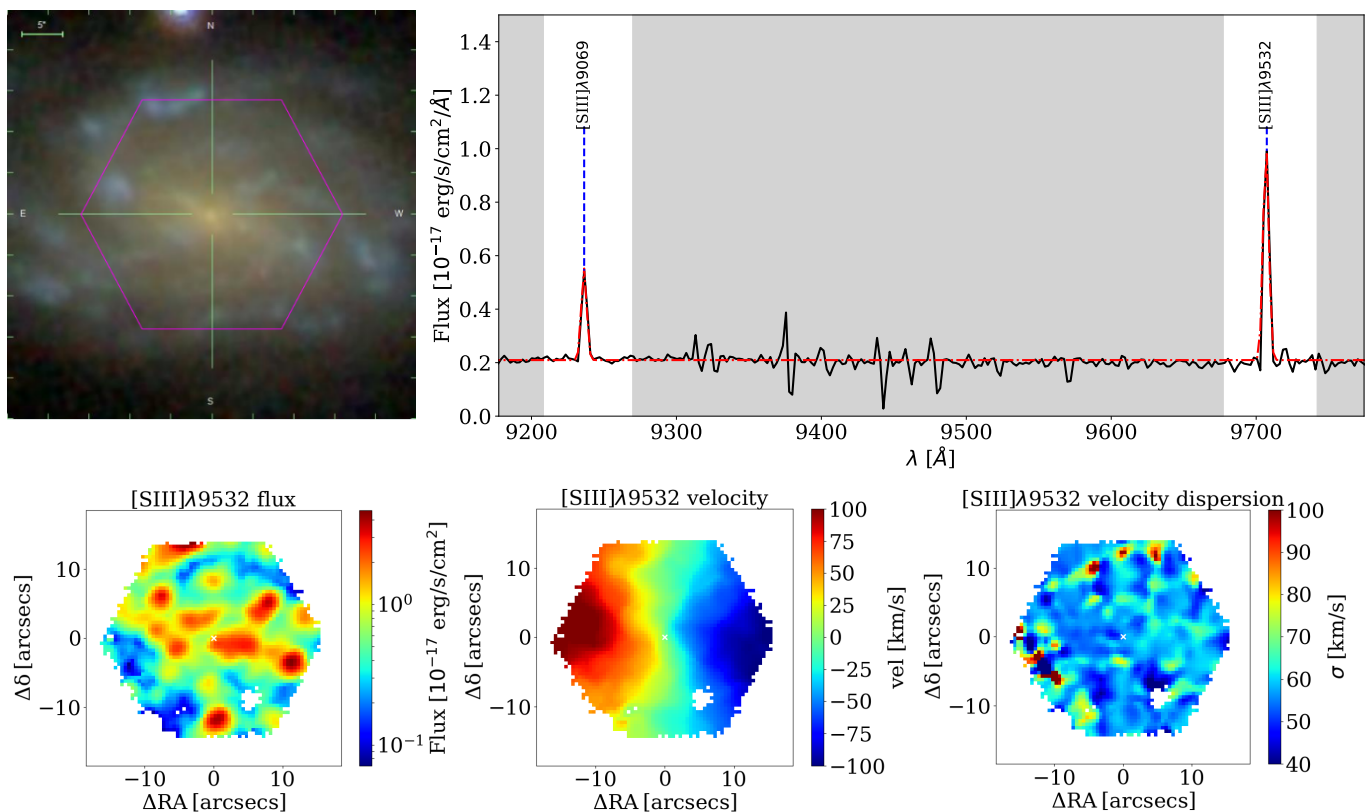


Fig. 1. Top left: $g-r-i$ image composite from SDSS for MaNGA galaxy 8150-6103, with the MaNGA IFU hexagonal FoV overlaid. East is to the left. Top right: An example of our fitting procedure for the [S III] lines for one representative spaxel in this example galaxy. The black solid line is the observed spectrum, while the dashed-dotted red line is the best-fit. The regions in grey were masked before fitting. Bottom panels: [S III]λ9532 flux, velocity and velocity dispersion maps of MaNGA galaxy 8150-6103.

up to the [S III]λ9069 emission line. However, we find a larger discrepancy with respect to the other emission lines for the [S III]λ9532, likely associated with a failure in the extrapolation of the continuum performed by Pipe3D (S. F. Sánchez, private communication).

2.3. Signal-to-noise selection

In this work, we define the signal-to-noise of each emission line $S/N_{\text{line}} = \text{Flux}/\text{Err}_{\text{flux}}$, as in Belfiore et al. (2019). This quantity is equivalent to the classical amplitude-over-noise ratio often used for line detection. In order to obtain reliable measurements for the ISM parameters of interest we exclude from further analysis spaxel with $S/N(\text{H}\alpha) < 15$. We follow this approach, based on the work of Mannucci et al. (2010), because a high $S/N(\text{H}\alpha)$ ensures that the main optical lines are generally detected with $S/N > 1.5$ without introducing metallicity biases. According to Belfiore et al. (2019), the fluxes computed by the DAP with $S/N \leq 1.5$ are unreliable. We therefore consider them as upper limits. This cut on $S/N(\text{H}\alpha)$ selects 85% of the star-forming spaxels of the galaxy sample. In Appendix B, we show the S/N radial profiles for MaNGA galaxies as a function of stellar mass. Overall, all strong lines of interest have $S/N > 5$ at $R < 2 R_e$, except the [S III] lines, which are particularly weak ($S/N \sim 2-4$) at large radii and for massive galaxies.

Aside from emission from H II regions, galaxies are observed to contain low surface brightness diffuse ionised gas (DIG). The origin of this ionised gas emission is likely to be a combination of different processes, such as radiation leaking from classical H II regions, massive stars in the field and radiation from

hot evolved stars (Hoopes & Walterbos 2003; Oey et al. 2007; Zhang et al. 2017; Sanders et al. 2017; Wylezalek et al. 2018). In this work we only consider H II region models. It is therefore necessary to minimize the contribution of DIG to our observed line fluxes.

Previous works have demonstrated the existence of a tight relation between diagnostic line ratios and $\text{H}\alpha$ equivalent width (EW) in emission (e.g., Sánchez et al. 2014; Belfiore et al. 2016; Zhang et al. 2017; Lacerda et al. 2018; Vale Asari et al. 2019). Specifically, Lacerda et al. (2018) argue that $EW(\text{H}\alpha) < 3 \text{ \AA}$ traces emission from hot low-mass evolved stars (Stasińska et al. 2008), while gas with $EW(\text{H}\alpha) = 3 - 14 \text{ \AA}$ may include a mixture of DIG and emission from star forming regions. Because of our selection in BPT classification and signal-to-noise described above, virtually all the spaxels taken into account in this work have $EW(\text{H}\alpha) > 3 \text{ \AA}$, and are therefore dominated by flux from H II regions.

3. Methods

3.1. Bayesian approach to determining ISM properties

Our method to derive the oxygen abundance and the ionisation parameter of ionised nebulae is based on the software tool IZI presented by Blanc et al. (2015). In brief, IZI compares an arbitrary set of observed SELs (and their associated errors) with a grid of photoionisation models, calculating the joint and marginalised posterior probability density functions (PDFs) for $12 + \log(\text{O}/\text{H})$ and $\log(q)$. This method allows us to include flux upper limits (see Blanc et al. 2015 for details), and it pro-

vides a self-consistent way of inferring the physical conditions of ionised nebulae using all available information. In particular, this approach makes it straightforward to test the effect of either a particular choice of SELs (as commonly done in traditional metallicity diagnostics) or a particular set of photoionisation models.

For this work we have re-written the original IDL IZI code in Python and added several modifications to the original code. The main innovation of our revisited version of IZI is the simultaneous estimate of a third parameter, the gas extinction $E(B - V)$. The gas extinction along the line-of-sight towards star-forming regions can be directly probed with Balmer recombination line flux ratios, comparing the observed and intrinsic Balmer decrements (e.g. Calzetti 1997). $E(B-V)$ is usually derived assuming a fixed un-attenuated case B recombination, and generally an intrinsic Balmer decrement of $H\alpha/H\beta = 2.86$, appropriate for an electron density $n_e = 100 \text{ cm}^{-3}$ and electron temperature $T_e = 10^4 \text{ K}$ (Osterbrock 1989). The intrinsic ratio depends weakly on density, with $H\alpha/H\beta = 2.86 - 2.81$ over four orders of magnitude in electron density ($n_e = 10^2 - 10^6 \text{ cm}^{-3}$, Osterbrock 1989). However, the dependence on temperature is relatively larger, leading to $H\alpha/H\beta$ intrinsic ratio value between 3.04 - 2.75 for 5000 - 20000 K (Dopita et al. 2003). Consequently, adopting a single intrinsic Balmer ratio neglects the direct effect of metallicity and ionisation parameter on the temperature of the nebula. For instance, Brinchmann et al. (2004) pointed out that ignoring the metallicity-dependence of the case B $H\alpha/H\beta$ ratio leads to an overestimate of the dust attenuation by up to $\sim 0.5 \text{ mag}$ for the most metal rich galaxies (see e.g. Fig. 6 Brinchmann et al. 2004). Therefore, in this work we estimate dust extinction together with metallicity and ionisation parameter, assuming a foreground screen attenuation, a Calzetti attenuation law with $R_V = 4.05$ (see Calzetti et al. 2000) and adopting the intrinsic Balmer decrements self-consistently calculated within the photoionisation model grids. Another big advantage of inferring gas extinction, metallicity and ionisation parameter simultaneously is that we are self-consistently taking into account the covariance in dust-corrected line fluxes after applying a dust correction.

We make use of the Markov chain Monte Carlo (MCMC) Python package `emcee` to evaluate the PDF of the three parameters (Foreman-Mackey et al. 2013). Since photoionisation models cannot fully reproduce all observed line ratios, following Blanc et al. (2015), Kewley & Ellison (2008) and Dopita et al. (2013) we adopt a systematic fractional error in the flux predicted by the photoionisation model of 0.1 dex, except for the $H\alpha$ line, for which we took into account 0.01 dex, in order to weight it more when constraining $E(B-V)$. This intrinsic uncertainty is the dominant source of the error term in IZI, being generally larger than the measurement error associated to observed fluxes. Consequently, signal-to-noise levels of the strong lines have a minor effect on the IZI output. Despite the differences from the publicly-available IDL code, for the rest of this work we refer to our rewritten and modified code as IZI unless otherwise noted.

As discussed by Blanc et al. (2015), it is not trivial to define a ‘best-fit’ solution for a specific parameter if its PDF is not Gaussian (e.g. strong asymmetries and/or multiple peaks). In these cases the mean is not a reliable estimator because it can be significantly different from the most likely solution, given by the mode. We choose as ‘best-fit’ value the marginalized median (i.e. 50th percentile) of the PDF for each parameter. The upper and lower errors of the best-fit solution are obtained by computing the 16th and 84th percentiles of the distribution, respectively,

and are defined as $\Delta_{up} = 84^{\text{th}} - 50^{\text{th}}$ and $\Delta_{down} = 50^{\text{th}} - 16^{\text{th}}$. If the PDF is Gaussian, these two values are equal and correspond to the standard deviation.

As our default photoionisation models set, we use the photoionisation model grids presented in Dopita et al. (2013) (D13 models hereafter). These models are computed with the `MAPPINGS-IV` code, which with respect to the previous version includes new atomic data, an increased number of ionic species treated as full non-local-thermodynamic-equilibrium multilevel atoms, and the ability to use electron energy distributions that differ from a simple Maxwell-Boltzmann distribution (Nicholls et al. 2013; Dopita et al. 2013). The grids that we use here are, however, calculated assuming a Maxwell-Boltzmann distribution, in light of the ongoing controversy on whether the use of alternative distributions is justified for H II regions Draine & Kreisich (2018).

In D13 models, the input ionising spectrum is computed through the population synthesis code `STARBURST99` (Leitherer et al. 1999), taking into account the Lejeune/Schmutz extended stellar atmosphere models (Schmutz et al. 1992; Lejeune et al. 1997), a constant star formation history (SFH), a Salpeter initial mass function (IMF, lower and upper mass cut-off at 0.1 M_{\odot} and 120 M_{\odot} , respectively), and an age of 4 Myr. D13 models are isobaric with an electron density $n_e \sim 10 \text{ cm}^{-3}$ and are computed for a spherical geometry. The assumed gas phase abundances are taken from Asplund et al. (2009), except for nitrogen and carbon. For these elements empirical fitting functions as a function of O/H are adopted (see Table 3 in Dopita et al. 2013). Furthermore, D13 models include dust physics and radiative transfer, assuming a population of silicate grains following Mathis et al. (1977) size distribution and a population of small carbonaceous grains within the ionised regions, as described in detail in Dopita et al. (2005). The metallicities vary in the range $12 + \log(\text{O}/\text{H}) = [7.39 - 9.39]$ (the solar oxygen abundance is 8.69), while the ionisation parameter varies in the range $\log(q) = [6.5 - 8.5]$. Intrinsic Balmer decrement values vary in the range $= [2.85 - 3.48]$, and are systematically higher than the standard Case B recombination value, as reported by Dopita et al. (2013).

In Fig. 2 we show as an example the comparison between the [N II]- and [S II]-BPT diagrams for our sample of MaNGA star-forming spaxels with the grid of D13 models described above. The dashed curve represents the demarcation line defined by Kauffmann et al. (2003) (Ka03), while the solid curve is the theoretical upper limit on SF line ratios proposed by Kewley et al. (2001) (Ke01). The dotted line, instead, is the boundary between Seyferts and low-ionisation (nuclear) emission-line regions (LI(N)ERs) introduced by Kewley et al. (2006). We noticed that [S II] lines are predicted to be weaker by $\sim 0.1 \text{ dex}$ (see Fig. 2) than observed, as already reported in Dopita et al. (2013) (a lower discrepancy is observed also between observed and modelled [N II]/ $H\alpha$ line ratios). This is due to the fact that [S II] ions are much more sensitive than [N II] ions to the diffuse radiation field in H II regions (Dopita et al. 2006a; Kewley et al. 2019). This issue is also discussed in Levesque et al. (2010), where the authors suggest that their models probably do not produce sufficient flux in the far-ultraviolet ionising spectrum. They argue that [S II] requires a larger partially ionised zone generated by a harder radiation field than the one present in the models.

Considering the above caveats, the optical line ratios in MaNGA spaxels are generally well-reproduced by the D13 models as ensembles. We have also reproduced all the diagnostics plots based on optical emission lines presented in Dopita et al. (2013) and find the MaNGA data global distribution to be well-

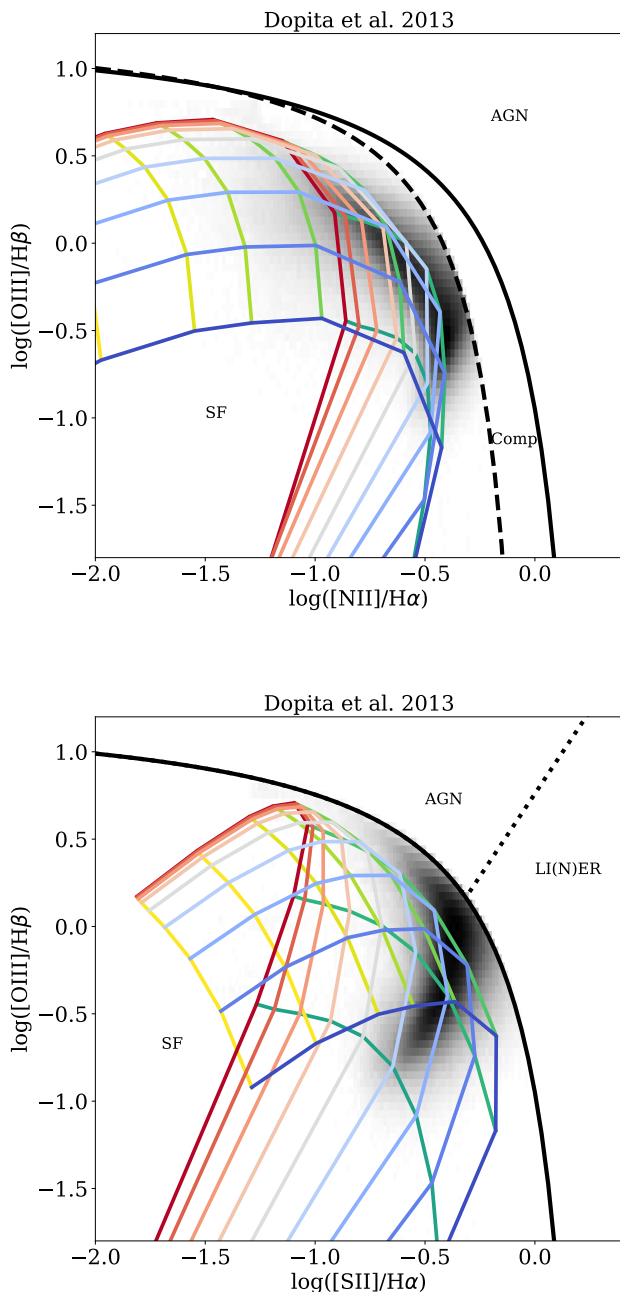


Fig. 2. [N II]- and [S II]-BPT diagrams for our sample of MaNGA spaxels compared with D13 models, for metallicities in the range [7.39–9.39] (increasing from yellow to green) and ionisation parameters in the range [6.5–8.5] (redder means higher $\log(q)$ and bluer lower $\log(q)$). D13 models generally well-reproduce the observed line ratios in MaNGA spaxels as ensembles.

covered by the model grids. As a caveat, we stress that this test does not demonstrate whether single galaxies are also well-reproduced by the models in all the diagnostic plots.

3.2. The failure of photoionisation models in reproducing the observed [S III] lines

Stasińska (2006) suggested that $\text{S3O3} = [\text{S III}]_{\lambda\lambda 9069, 9532} / [\text{O III}]_{\lambda\lambda 4959, 5007}$ versus S3S2 repre-

sents a useful diagnostic plot, where the horizontal axis is mostly tracing metallicity while the vertical axis traces the ionisation parameter. Indeed, S3O3 is found to vary monotonically with metallicity, similarly to the more commonly employed O3N2 diagnostic (Dopita et al. 2013).

Fig. 3 shows S3O3 versus S3S2 of all the selected MaNGA spaxels (black contours), the brightest MaNGA star-forming regions [$EW(\text{H}\alpha) > 100 \text{ \AA}$] (red contours) and single H II regions analysed in Kreckel et al. (2019)² within eight galaxies from the Physics at High Angular resolution in Nearby Galaxies³ (PHANGS) survey (grey dots), in comparison with different sets of photoionisation models (described below). The observed line ratios are corrected for reddening assuming a Calzetti attenuation law with $R_V = 4.05$ (see Calzetti et al. 2000) and adopting the intrinsic Balmer decrement of 2.86. As shown in the top left panel of Fig. 3, the D13 models largely overestimate the [S III] fluxes (black contours), being consistently shifted both horizontally and vertically with respect to our data. In order to test whether this discrepancy is caused by any specific feature of the D13 models, we consider three other sets of photoionisation models, based on different ingredients and assumptions: the Levesque et al. (2010) models (Fig. 3, upper right panel), two different versions of the Byler et al. (2017) models (Fig. 3, lower left and right panels), and the Pérez-Montero (2014) models.

Levesque et al. (2010) (L10) photoionisation models are computed with MAPPINGS-III, adopting a version of the STARBURST99 population synthesis code (Vázquez & Leitherer 2005) that uses the Pauldrach/Hillier stellar atmosphere models (Pauldrach et al. 2001; Hillier & Miller 1998), and evolutionary tracks produced by the Geneva group (Schaller et al. 1992). Therefore, these models are characterised by a detailed non local thermal equilibrium modelling of metal line blanketing, which significantly affects the shape of the ionising spectrum, unlike the Lejeune/Schmutz models used in D13.

Byler et al. (2017) (B17) photoionisation models, instead, are obtained with version 13.03 of CLOUDY (Ferland et al. 2013), using the Flexible Stellar Population Synthesis code (FSPS; Conroy et al. 2009), based on Padova+Geneva and MESA isochrones and stellar tracks (MIST; Choi et al. 2016; Dotter 2016) evolutionary tracks, where the latter include stellar rotation. Stellar rotation affects stellar lifetimes, luminosities, and effective temperatures through rotational mixing and mass loss, implying harder ionising spectra and higher luminosities (see Choi et al. 2016; Byler et al. 2017 for further details). B17 models are characterised by a spherical shell cloud geometry and a constant gas density of $n_e = 100 \text{ cm}^{-3}$. The assumed gas phase abundances are taken from Dopita et al. (2000), which are based on the solar abundances from Anders & Grevesse (1989).

Finally, Pérez-Montero (2014) (PM14) photoionisation models are obtained with version 13.03 of CLOUDY (Ferland et al. 2013) as well, assuming a plane-parallel geometry with a constant electron density of $n_e = 100 \text{ cm}^{-3}$. The input ionising spectrum is derived from PopStar (Mollá et al. 2009) evolutionary synthesis models. The assumed gas phase abundances are taken from Asplund et al. (2009), except for nitrogen, that is considered a free parameter, varying in the range [-2,0]. The grid shown in Fig. 3 corresponds to $\log(\text{N/O}) = -0.875$, close to the solar value $\log(\text{N/O}) = -0.86$ (Asplund et al. 2009; note that this choice does not take into account the detailed shape of the N/O versus O/H sequence, but this is of little importance to the [S III] line fluxes).

² Private communication.

³ <https://www.phangs.org>

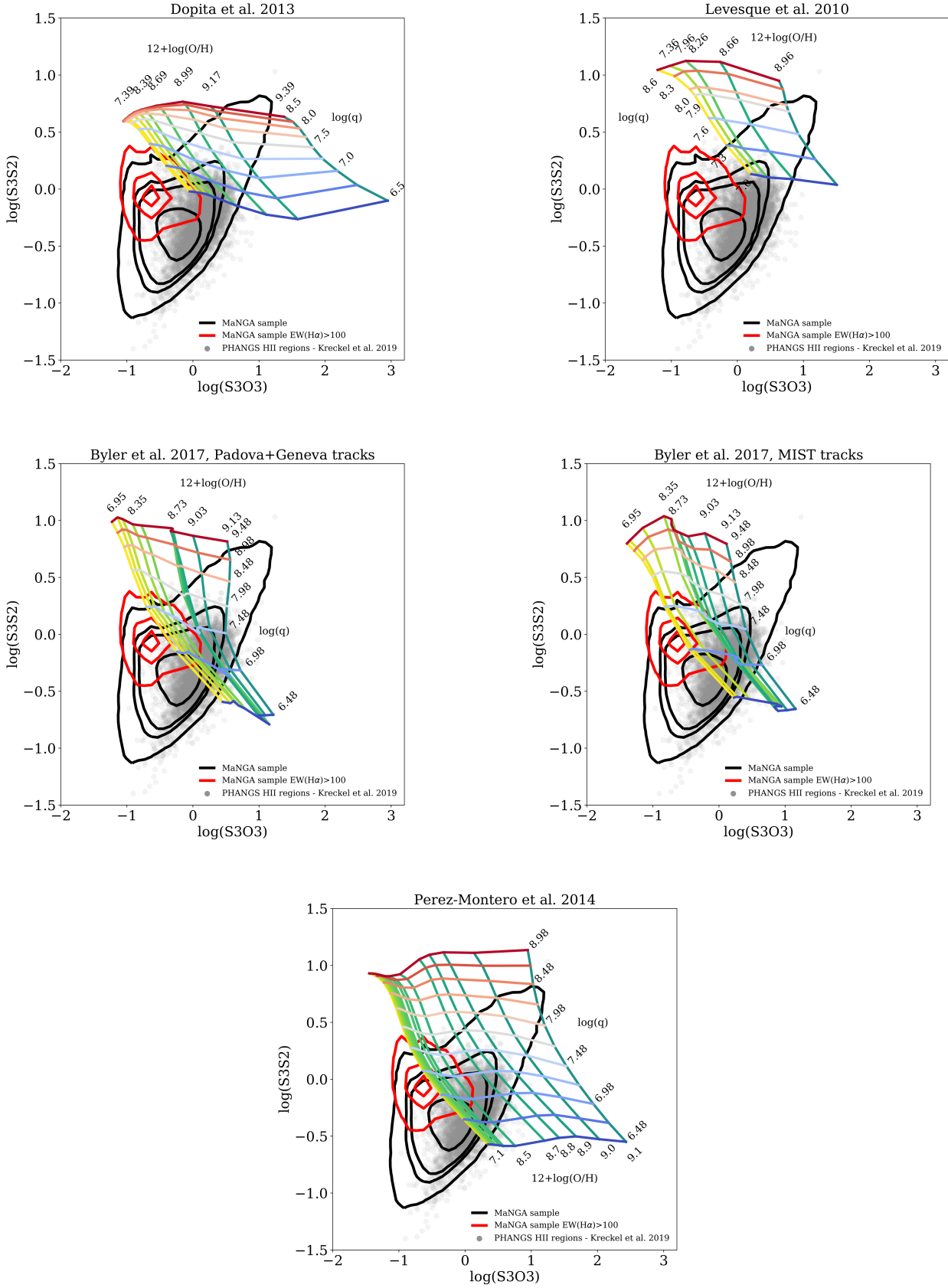


Fig. 3. $[S\ III]/[O\ III]$ versus $[S\ II]/[O\ II]$ diagnostic diagrams introduced by Stasińska (2006) showing the density contours for all the star-forming spaxels of our sample (in black), with superimposed Dopita et al. (2013), Levesque et al. (2010), Byler et al. (2017) pdva+geneva, Byler et al. (2017) MIST, and Pérez-Montero (2014) models respectively. Metallicity increases horizontally from yellow to green, while ionisation parameter increases vertically [redder means higher $\log(q)$ and bluer lower $\log(q)$]. The red contours correspond to the brightest MaNGA star-forming regions [$EW(H\alpha) > 100$], while the grey dots are the H II regions analysed by Kreckel et al. (2019) with the PHANGS survey. Current photoionisation models fail to reproduce the observed $[S\ III]$ lines.

Interestingly, taking into account these different sets of photoionisation models does not resolve the discrepancy with our observations. The Levesque et al. (2010) grids are even more further removed from the data than the Dopita et al. (2013) grids. The two Byler et al. (2017) and Pérez-Montero (2014) grids appear to provide a better fit, since they predict $\log([\text{S III}]/[\text{S II}])$, line ratios as low as ~ -0.75 , in better agreement with the data, but still overestimate $\log([\text{S III}]/[\text{O III}])$. As a consequence of the latter fact, only low-metallicity models can be superimposed with the data.

We then test whether this observed discrepancy persists in the high-S/N regime. This regime is also worth exploring because low surface brightness and low $EW(\text{H}\alpha)$ regions in MaNGA galaxies tend to be increasingly contaminated by DIG, which is known to display different line ratios than classical H II regions. We therefore select only the brightest star-forming regions by looking for spaxels with $EW(\text{H}\alpha) > 100 \text{ \AA}$ (red contours), and still find a significant difference between observed and predicted fluxes.

Since MaNGA data have a kpc scale resolution, H II regions, characterised by sizes between 10 – 100 pc (Azimlu et al. 2011; Gutiérrez et al. 2011; Whitmore et al. 2011) cannot be resolved, and spatial averaging could lead to loose significant information. In order to show that this issue is not the cause of the discrepancy between models (designed for H II regions) and the data with regards to the [S III] lines, we also take into account single H II regions analysed by Kreckel et al. (2019) with the PHANGS survey (grey dots in Fig. 3). For these galaxies, we estimated the [S III] λ 9069,9532 flux from the extinction-corrected [S III] λ 9069 reported in Kreckel et al. (2019), assuming an intrinsic value between the two [S III] lines of 2.47 (Luridiana et al. 2015). The fact that the discrepancy holds also in this case allows also to exclude that it is related to the presence of DIG.

The discrepancy between observed and modelled [S III] fluxes has been already reported in the literature (e.g. Garnett 1989; Dinerstein & Shields 1986; Ali et al. 1991). Specifically, Garnett (1989) showed that the [S III]/[S II] ratio was over-predicted by their photoionisation models. Their models produced [O II]/[O III] ratios comparable to observations, suggesting the discrepancy may be due to limitations in modelling stellar atmospheres and/or in the atomic data for sulfur. Very recently, Kewley et al. (2019) discuss the use of [S III]/[S II] as an ideal ionisation parameter diagnostic, but come to the same conclusions with regards to the limitations in the modelling effort so far. Kewley et al. (2019) however, only discuss modelling issues with regards to the [S II] lines, since no large sample of galaxies with [S III] observations was available to date. In this work we finally provide such a dataset and confirm that the discrepancy between models and observations of the [S III] lines is a lingering problem, which persists in observations of a large sample of local galaxies and latest-generation photoionisation models based on independent state-of-the-art codes.

3.3. Applying IZI to the MaNGA data

Given that the [S III] lines are not well-reproduced by photoionisation models, we first run IZI excluding the [S III] line fluxes. In particular, we consider the fluxes of [O II] λ 3726,29, H β , [O III] λ 4959,5007, [N II] λ 6548,84, H α , [S II] λ 6717 and [S II] λ 6731 and make use of the D13 models. We stress that, even though $E(\text{B-V})$ is derived assuming a screen attenuation, the IZI output takes into account also the internal dust taken into account in D13 models (see Sec. 3.1). Indeed, the internal dust

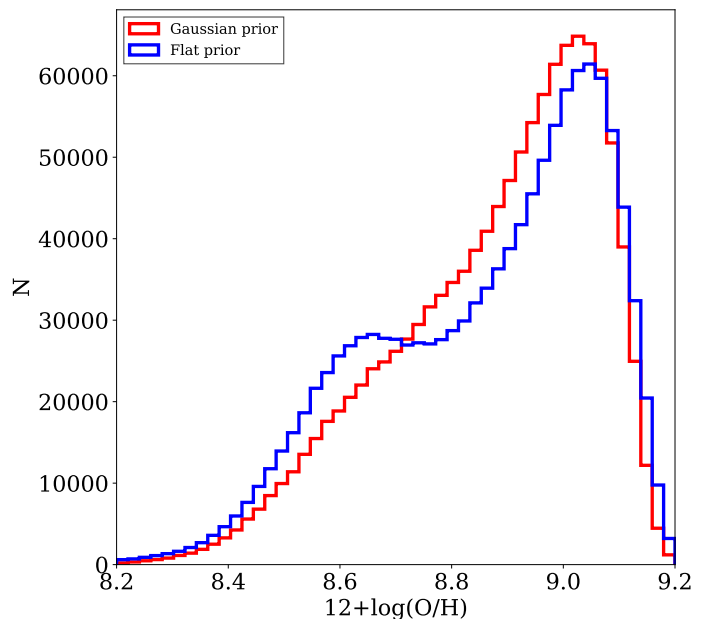


Fig. 4. Distribution of the best-fit values of $12+\log(\text{O}/\text{H})$ for all MaNGA spaxels considered in this work. Metallicities are derived by IZI with a Gaussian (red) and a flat (blue) prior on the ionisation parameter, respectively. Specifically, the mean of the Gaussian prior is given by the Diaz et al. (1991) calibration, that links [S III]/[S II] line and ionisation parameter.

modifies the thermal structure of the H II region, and thus the emission-line spectrum, particularly in the high-excitation regions, affecting the abundances derived by the model (e.g. Dopita et al. 2000). We assume uniform priors for metallicity and the $\log(q)$ within the range provided by the selected photoionisation models. The extinction $E(\text{B-V})$ is also assumed to follow a flat prior in the range [0, 1] mag. We have checked that adding the [S III] lines to the list of strong lines ratios does not change the IZI output. This is because the [S III] lines are so badly reproduced by the models that they are unable to provide useful information on the best-fit parameter values. If the [S III] lines are introduced in the fit they are characterised by a large χ^2 (10–25) compared to all other lines, highlighting how the D13 models are generally capable of reproducing all strong line ratios except those including [S III].

Fig. 4 shows in blue the histogram of the best-fit values of the metallicity obtained by IZI without taking into account the [S III] lines. Interestingly, the metallicity distribution tends to be bimodal, peaking at $12+\log(\text{O}/\text{H}) \sim 9$ and at $12+\log(\text{O}/\text{H}) \sim 8.6$, with a gap around $12+\log(\text{O}/\text{H}) \sim 8.8$. As we discuss below, we argue that the peak at $12+\log(\text{O}/\text{H}) \sim 8.6$ could be due to an underestimation of metallicity, because of the degeneracy between $12+\log(\text{O}/\text{H})$ and $\log(q)$. The results of taking into account the [S III]/[S II] line ratio to determine the ionisation parameter are described in the next section and are shown with the red line.

In order to better visualise the origin of the bimodality in the metallicity distribution of spaxels and its possible relation to intrinsic degeneracies in the fitting process, we show as an example different tests performed on one spaxel of the galaxy 7990-12703, chosen as a random spaxel with best-fit metallicity close to the lower-metallicity peak in the bimodal metallicity distribution of all MaNGA spaxels (Fig. 4, $12+\log(\text{O}/\text{H}) = 8.7$). In the upper panel of Fig. 5 we show in blue the posterior PDFs of $12+\log(\text{O}/\text{H})$, $\log(q)$ and $E(\text{B-V})$, inferred by IZI without taking into account the [S III] lines. Strong degeneracy be-

tween metallicity and ionisation parameter is evident from the figure. The $12+\log(\text{O}/\text{H})$ PDF is found to be very wide, characterised by likely values in the range $[8.6, 8.9]$ (best-fit median value of $12+\log(\text{O}/\text{H}) = 8.7$). We believe that the inability of constraining the metallicity in this example is due to the lack of a strong ionisation parameter diagnostic capable of tightly constraining $\log(q)$, as suggested by the wide PDF of this parameter, covering the range $[6.8, 7.4]$. The lower panel of Fig. 5 displays in green and orange the PDFs calculated using only $[\text{O II}]\lambda\lambda 3726, 29$, $\text{H}\beta$ and $[\text{O III}]\lambda\lambda 4959, 5007$ (i.e., R23), and $\text{H}\beta$, $[\text{O III}]\lambda\lambda 4959, 5007$, $[\text{N II}]\lambda\lambda 6548, 84$ and $\text{H}\alpha$, (i.e. O3N2), respectively. In both cases, there is a clear degeneracy between a low-metallicity low-ionisation parameter and a high-metallicity, high-ionisation parameter solution. Indeed, R23 is known to be double-valued (e.g., Pagel et al. 1979; Dopita et al. 2006a). O3N2 is commonly used as metallicity diagnostic, but it carries a strong dependence on the ionisation parameter, because of the very different ionisation potentials of N^+ (14.5 eV) and O^{++} (35.1 eV) (Alloin et al. 1979). This leads to a systematic underestimation of $12+\log(\text{O}/\text{H})$ for higher ionisation parameters and overestimation of $12+\log(\text{O}/\text{H})$ in regions characterised by lower ionisation parameter values (e.g. Cresci et al. 2017; Krühler et al. 2017).

3.4. Imposing a prior on the ionisation parameter based on the $[\text{S III}]/[\text{S II}]$ ratio

The discrepancy between model predictions and $[\text{S III}]$ emission line fluxes prevents us from introducing them directly in our method together with all the other emission lines. Hence, in order to understand if and to what extent the $[\text{S III}]\lambda\lambda 9069, 9532$ lines can help in the determination of the ionisation parameter and in breaking the degeneracy with metallicity illustrated in Fig. 4 and Fig. 5, we compute a second run of IZI using the $[\text{S III}]/[\text{S II}]$ ratio to set a Gaussian prior on $\log(q)$. Specifically, we choose to set the mean of this Gaussian prior by linking $[\text{S III}]/[\text{S II}]$ and ionisation parameters via a commonly-used calibration obtained by using a large grid of single-star photoionisation models by Diaz et al. (1991) (D91 hereafter),

$$\log(q) = -1.68 \times \log([\text{S II}]/[\text{S III}]) + 7.49, \quad (2)$$

taking into account a standard deviation of 0.2 dex. Recently, Morisset et al. (2016) recalibrated this relation using an updated version of CLOUDY (Ferland et al. 2013) and atomic data, finding reasonable agreement with Eq. 2. This approach allows the $[\text{S III}]$ lines to add extra information to the fit, while at the same time not fully constraining $\log(q)$ to the value obtained via the D91 calibration. We stress that since we do not fix the ionisation parameter to the value inferred by Diaz et al. (1991), the use of Morisset et al. (2016) calibration would not change our results, given that Diaz et al. (1991) and Morisset et al. (2016) are reasonably consistent within ± 0.2 dex. The Gaussian prior can be applied only in those spaxels in which $[\text{S III}]\lambda 9532$, $[\text{S II}]\lambda 6717$, $[\text{S II}]\lambda 6731$, $\text{H}\alpha$ and $\text{H}\beta$ are observed with $S/N > 1.5$, which are $\sim 80\%$ of the total.

Fig. 6 shows $\log(q)$ inferred with IZI with the flat prior on the ionisation parameter as a function of the observed $\log(\text{S3S2})$. The green dashed line illustrates the $\log(q)$ values obtained with Eq. 2, while the green dotted lines represent the ± 0.2 dex scatter around this relation. D13 models are shown for comparison (from red to blue going from high to low metallicity). Given the range of $\log(\text{S3S2})$ observed in our data, the ionisation parameters obtained via the D91 calibration are broadly in the same

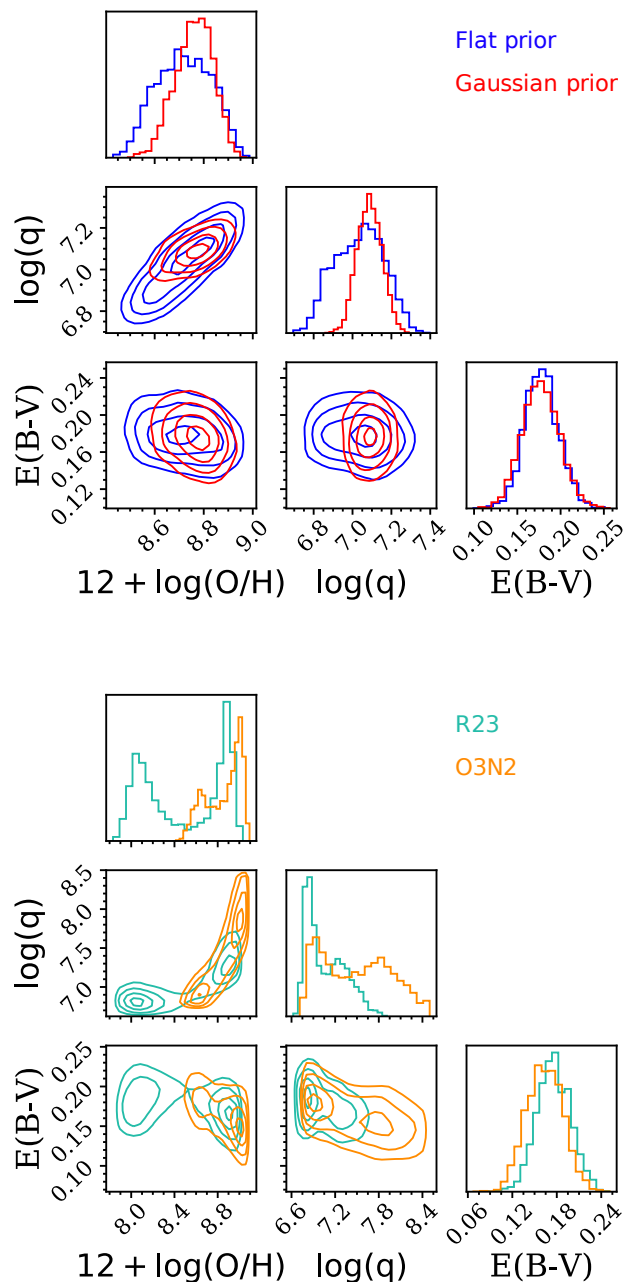


Fig. 5. Top panel: Posterior PDFs relative to $12+\log(\text{O}/\text{H})$, $\log(q)$ and $E(\text{B}-\text{V})$, inferred with a Gaussian (red) and a flat (blue) prior on the ionisation parameter, respectively, with D13 models, for a single spaxel of the galaxy 7990-12703. Bottom panel: Posterior PDFs relative to the three parameters, inferred only taking into account $[\text{O II}]\lambda\lambda 3726, 29$, $\text{H}\beta$ and $[\text{O III}]\lambda\lambda 4959, 5007$ (i.e., R23, in green), and $\text{H}\beta$, $[\text{O III}]\lambda\lambda 4959, 5007$, $[\text{N II}]\lambda\lambda 6548, 84$ and $\text{H}\alpha$, (i.e. O3N2, in orange), respectively.

range as the ionisation parameter inferred by IZI using all other strong lines except $[\text{S III}]$ within ± 0.2 dex.

The reason why the D91 calibration, which is itself based on photoionisation models, is in better agreement with the data than all the other models considered in the previous section is still an unresolved problem. The main discrepancy between D13, D91 and Morisset et al. 2016 photoionisation models, however, could be related to the input ionising spectrum (see also Sec. 4.1

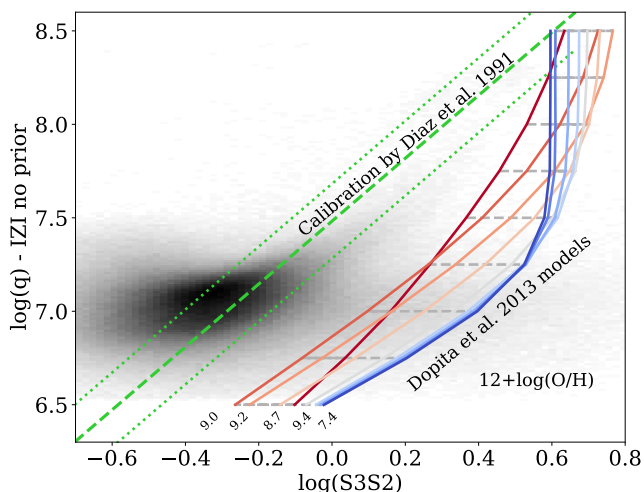


Fig. 6. The distribution of $\log(q)$ as a function of $\log(\text{S3S2})$ inferred with IZI with a flat prior on the ionisation parameter is shown in shades of grey. The green dashed line shows the $\log(q)$ values obtained with Eq. 2 (Diaz et al. (1991)), while the green dotted lines represent the ± 0.2 dex scatter around this relation. D13 models are shown in colour (red-blue, going from higher to lower metallicity).

and Fig. 5 in Morisset et al. 2016), but also to the underlying assumptions of the models (e.g. changes in atomic data, inclusion/exclusion of dust physics).

The differences between our two IZI runs (with a Gaussian and a flat prior on the ionisation parameter) can be appreciated from the three panels of Fig. 7. These figures compare the best-fit values (i.e. the median of the PDF computed by IZI, see Sec. 3.1) of metallicity, ionisation parameter and gas extinction obtained without taking into consideration the [S III] lines (x-axis) and imposing a Gaussian prior on $\log(q)$ based on S3S2 (y-axis), respectively. The metallicity distributions of the two runs are consistent at values $12+\log(\text{O}/\text{H}) > 8.9$, but below this threshold metallicities inferred by the IZI run with the Gaussian prior tend to be higher than those inferred by IZI with the flat prior. The distribution of ionisation parameters of all considered spaxels is found to be wider when taking into account the prior, since the best-fit values tend to be lower for $\log(q) < 7$ and higher for $\log(q) > 7.2$. Finally, as expected, the prior on the ionisation parameter has no effect on the gas extinction.

Coming back to Fig. 4, the histogram of the best-fit values of the metallicity obtained by the IZI run with the Gaussian prior on the ionisation parameter is shown in red. Note that the bimodality discussed in Sec. 3.3 disappears when the Gaussian prior is imposed. Indeed, in the upper panel of Fig. 5, the degeneracy is broken introducing the Gaussian prior based on the Diaz calibration (shown in red as well), in which a higher metallicity (8.8 vs 8.7) and a higher ionisation parameter (7.1 vs 7.0) solution is preferred.

As explained in Sec. 3.1, the errors provided by IZI are obtained by computing the 16th, 50th and 84th percentiles of the PDFs, and are defined as $\Delta_{up} = 84^{\text{th}} - 50^{\text{th}}$ and $\Delta_{down} = 50^{\text{th}} - 16^{\text{th}}$. The difference between Δ_{up} and Δ_{down} indicates how much these PDFs differ from a symmetric distribution. In general this difference would be greater than zero if the distribution is tailed towards higher values with respect to its median value, considered as the best-fit, and vice-versa. Fig. 8 shows the distribution of the difference between Δ_{up} and Δ_{down} for the metallicity (left panel) and ionisation parameter (right panel), in the case

with a flat (blue) and a Gaussian (red) prior on the ionisation parameter, for all the spaxels considered in this work. In the case with the flat prior, these distributions are shifted towards negative values both for $12+\log(\text{O}/\text{H})$ and $\log(q)$ $\Delta_{up} - \Delta_{down}$, meaning that the majority of the spaxels have an asymmetric PDF tailed towards lower values with respect to the best-fit. Moreover, these distributions show a cut-off around 0 (this is more visible for $12+\log(\text{O}/\text{H})$), with a considerable tail at positive values to ~ 0.075 , implying that some spaxels have an asymmetric PDF tailed towards higher values with respect to the best-fit. This leads to the bimodality discussed above.

In the case with the Gaussian prior, the $\log(q)$ $\Delta_{up} - \Delta_{down}$ distribution is almost Gaussian, centered on zero, mirroring the prior itself. The metallicity distribution remains slightly shifted towards negative values (i.e. high values of metallicity), but shows a much less conspicuous tail compared to the case with the flat prior, indicating a general significant reduction in the effect of the $12+\log(\text{O}/\text{H}) - \log(q)$ degeneracy.

Fig. 9 shows the metallicity inferred for each galaxy at $0.8 R_e$, obtained by interpolating the metallicity profile as a function of galactocentric distance. This characteristic metallicity is shown as a function of the total stellar mass, colour-coded on the basis of the ionisation parameter (also at $0.8 R_e$) for the case with the flat and the Gaussian prior on the ionisation parameter, respectively. We present the corresponding metallicity distributions as grey histograms on the right. We comment here on this well-known scaling relation between mass and metallicity (MZR, Lequeux et al. 1979; Tremonti et al. 2004) to highlight the importance of breaking the degeneracy between metallicity and ionisation parameter when investigating secondary trends.

As the left panel of Fig. 9 shows, in the case with the flat prior we find the hint of a bimodality in the metallicity distribution, shown in the grey histogram, with values around $12+\log(\text{O}/\text{H}) \sim 8.8$ being less probable. This feature creates a steeper slope for the mass-metallicity relation in the range $9.5 < \log(M_*/M_\odot) < 10$, with respect to the case with the prior, and in agreement with the even larger bimodality in the mass-metallicity relation derived by Blanc et al. (2019) with IZI and the Levesque et al. 2010 models.

More strikingly, at fixed mass there is a strong correlation between metallicity and ionisation parameter (a smoothing has been applied to the colour-coding for ease of visualisation, using the LOESS recipe from Cappellari et al. 2013). This correlation disappears when a Gaussian prior based on [S III]/[S II] is used (right panel of Fig. 9). We argue, therefore, that this secondary dependence of metallicity on $\log(q)$ seen in the case with the flat ionisation parameter prior is solely due to the degeneracy between the two parameters.

In Tab. 3.4 we report the best-fit parameter values for the MZR shown in Fig. 9, using the new parametrisation proposed in Curti et al. (2019b) (C19):

$$12 + \log(\text{O}/\text{H}) = Z_0 - \gamma/\beta \times \log\left(1 + \left(\frac{M}{M_0}\right)^{-\beta}\right) \quad (3)$$

In this equation, Z_0 is the metallicity at which the relation saturates, quantifying the asymptotic upper metallicity limit, while M_0 is the characteristic turnover mass above which the metallicity asymptotically approaches the upper metallicity limit (Z_0). At stellar masses $M_* < M_0$, the MZR reduces to a power law of index γ . In Eq. 3, β quantifies how “fast” the curve approaches its saturation value. The parameters that we obtain for the two different MZRs, shown on the left and right of Fig. 9, are consistent within the errors, and the scatter around the best-fit relations are 0.12 dex and 0.10 dex, respectively.

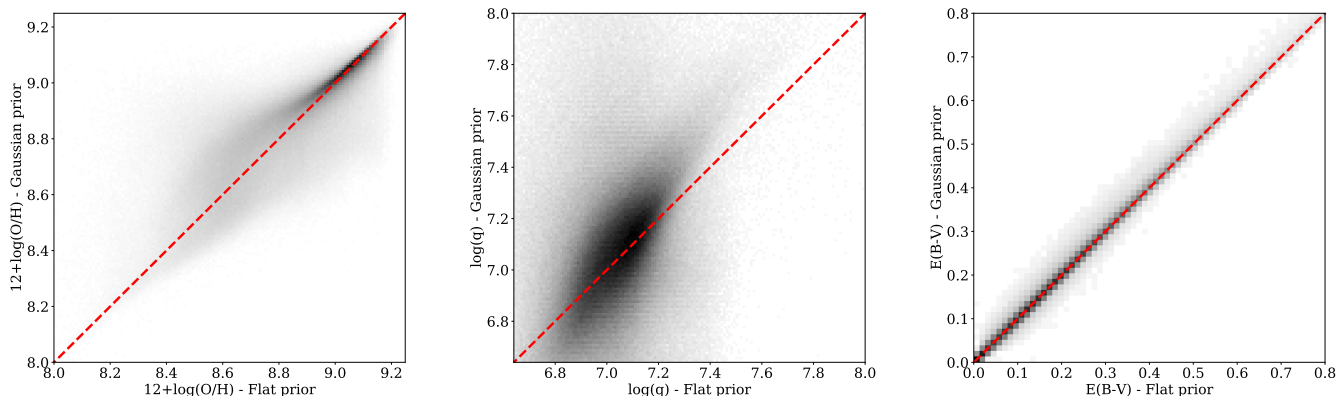


Fig. 7. Comparison between the results obtained with IZI with a flat (x-axis) and a Gaussian (y-axis) prior on the ionisation parameter, for metallicity, ionisation parameter and gas extinction, respectively. The red dashed line represents the one-to-one relation.

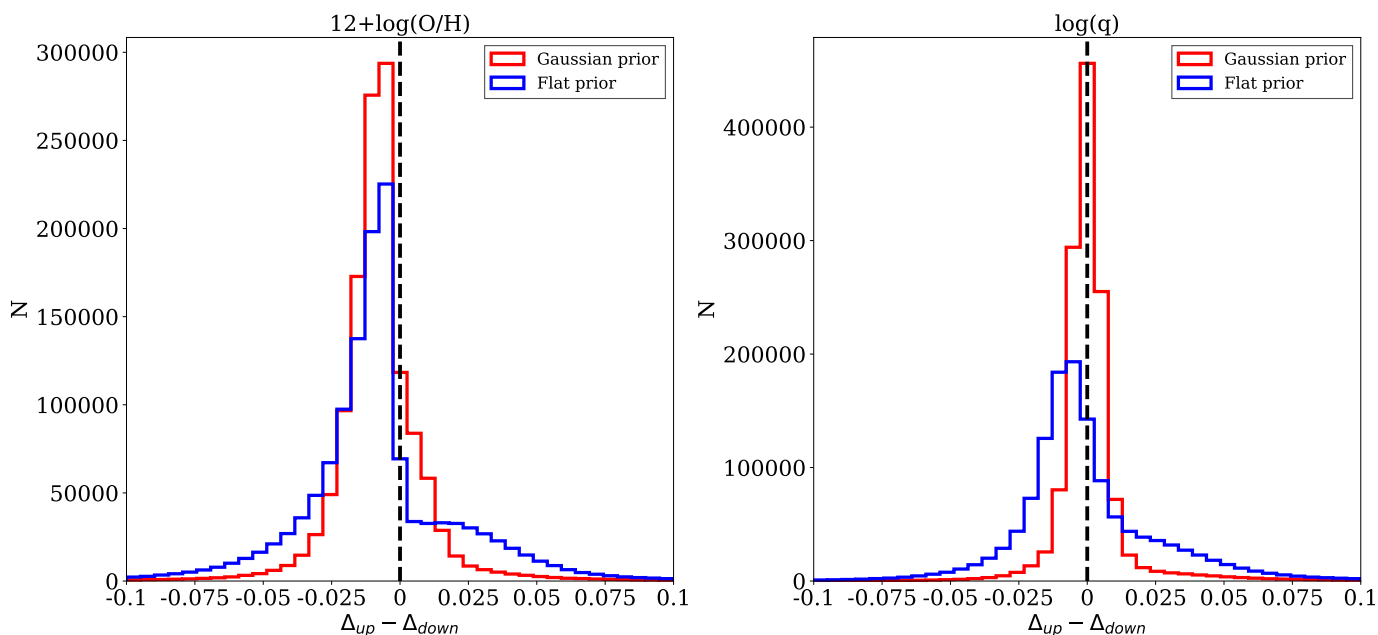


Fig. 8. Distribution of the difference between $\Delta_{up} = 84^{\text{th}} - 50^{\text{th}}$ and $\Delta_{down} = 50^{\text{th}} - 16^{\text{th}}$ for the metallicity (left panel) and ionisation parameter (right panel), in the case with a flat (in blue) and a Gaussian (in red) prior on the ionisation parameter, respectively, for all the spaxels of all the galaxies.

Table 1. Best-fit values for the parameters of the MZR shown in the right panel of Fig. 9 derived with IZI, putting a Flat and a Gaussian prior on the ionisation parameter based on $[\text{S III}]/[\text{S II}]$, assuming the new parametrisation proposed in Curti et al. (2019b) (Eq. 3).

MZR C19 - Flat prior			
Z_0	M_0/M_\odot	γ	β
$9.07^{+0.06}_{-0.04}$	$9.3^{+0.1}_{-0.2}$	$1.3^{+0.4}_{-0.4}$	$1.1^{+0.5}_{-0.4}$
MZR C19 - Gaussian prior			
Z_0	$\log(M_0/M_\odot)$	γ	β
$9.06^{+0.05}_{-0.04}$	$9.3^{+0.1}_{-0.2}$	$1.1^{+0.5}_{-0.4}$	$1.2^{+0.5}_{-0.4}$

In order to show the reliability of our method, in App. C, we show the comparison between the observed value of $H\alpha$, $[\text{N II}]\lambda 6584$, $[\text{O II}]$, $[\text{O III}]\lambda 5007$, $[\text{S II}]\lambda 6717$, $[\text{S II}]\lambda 6731$ and $[\text{S III}]\lambda 9532$ and the fluxes of the the best-fitting model predicted by IZI (all normalised to $H\beta$), taking into account D13 models

and a Gaussian prior on the ionisation parameter, as a function of the Petrosian effective radius and stellar mass, for all the spaxels of all the galaxies taken into account. Overall, the stellar-mass- and radius-dependent variations lie in the range $[-0.1, 0.1]$ dex, meaning that they are all consistent within the assumed uncertainty of 0.1 dex (0.01 dex for $H\alpha$) for the photoionisation models. As expected, this does not hold for the $[\text{S III}]\lambda 9532$ emission line, that is largely overestimated by IZI, with differences between observed and predicted fluxes up to 0.8 dex.

4. Metallicity, ionisation parameter and gas extinction in MaNGA galaxies

In this section we show the results obtained with the IZI run which makes use of the Gaussian prior on the ionisation parameter, as described in Sec. 3. In all the plots, only the spaxels classified as star-forming according to both the $[\text{N II}]$ - and the $[\text{S II}]$ -

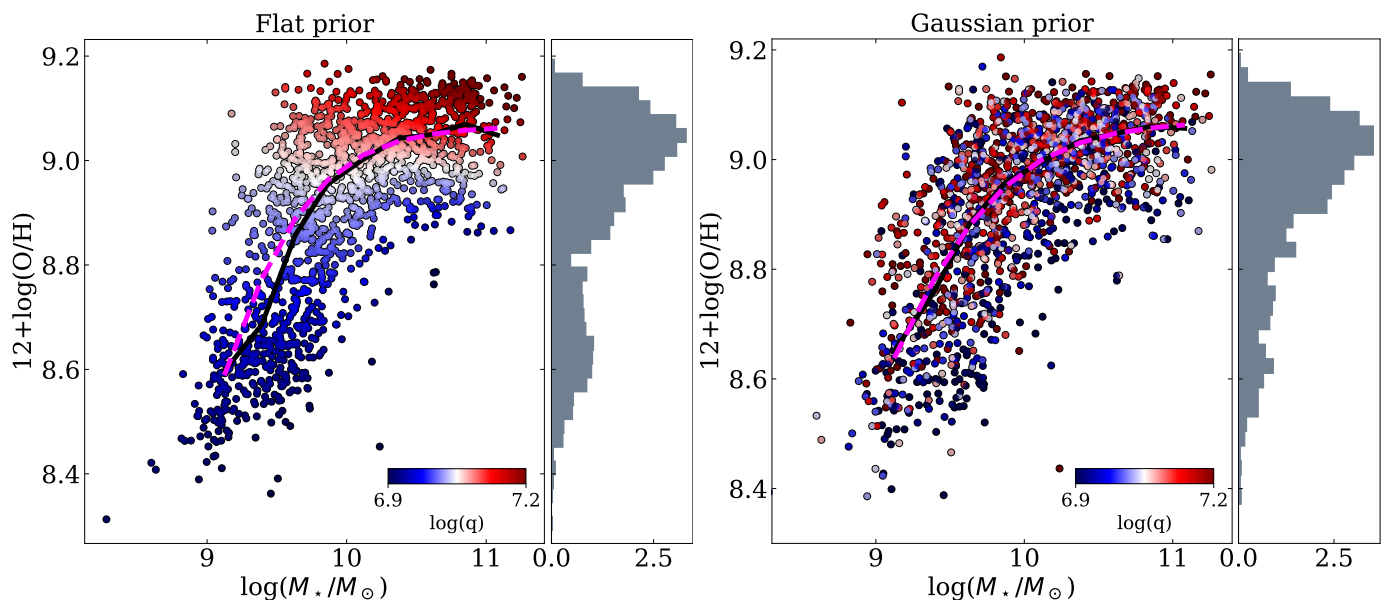


Fig. 9. The mass-metallicity relation for the MaNGA star-forming galaxies considered in this work without using the [S III] lines (left) and by using the [S III] lines via an ionisation parameter prior as discussed in the text (right). Metallicities are computed for each galaxy at $0.8 R_e$. The colour-coding indicates the ionisation parameter (at $0.8 R_e$). A histogram of the metallicity distributions for all galaxies is shown in grey on the right. In the case where the [S III] lines are not used (left panel) there is a striking correlation at fixed mass between the metallicity and ionisation parameter. To visually highlight this correlation the colour-coding has been smoothed according to the LOESS recipe of Cappellari et al. (2013). The solid black lines show the median metallicity in bins of M_* , while the dashed magenta lines are the best-fit using the parametrisation proposed in Curti et al. (2019b).

BPT diagrams with $S/N(H\alpha) > 15$ and in which the prior based on the S3S2 line ratio can be used are shown.

4.1. Example maps for low- and high-mass galaxies

Fig. 10 and Fig. 11 show an example of a low-mass (8147-9102, $\log(M_*/M_\odot) = 9.10$) and a high-mass (9041-12701, $\log(M_*/M_\odot) = 10.93$) galaxy in our sample. The quantities displayed are: $g - r - i$ image composite from SDSS with the MaNGA hexagonal FoV overlaid, the logarithm of equivalent width of $H\alpha$ [$EW(H\alpha)$], the $\log(S3S2)$ and $\log(O3O2)$ line ratios, the IZI best-fit metallicity $12 + \log(O/H)$, ionisation parameter $\log(q)$ and gas extinction $E(B-V)$, and the logarithm of the resulting luminosity of $H\alpha$ per spaxel corrected for extinction [$l(H\alpha)$].

In the low-mass galaxy, the S3S2 line ratio map, used as a prior for the ionisation parameter, and the O3O2 line ratio map look very similar. Interestingly, both the S3S2 and O3O2 line ratios tend to trace the regions with higher values of $EW(H\alpha)$ and $l(H\alpha)$, and thus show a clumpy distribution.

On the other hand, in the high-mass galaxy the S3S2 and O3O2 maps look qualitatively different. The S3S2 line ratio map is clumpy with an enhancement in the eastern direction, while the O3O2 line ratio is higher in the center, but shows a roughly flat profile over the FoV. The similarity between S3S2 line ratios and $EW(H\alpha)$ persists, while there is no clear correlation between S3S2 and $l(H\alpha)$. Indeed, the central regions in which $l(H\alpha)$ is enhanced are characterised by lower values of S3S2. The discrepancy between S3S2 and O3O2 in the high mass galaxy, could be due to the strong dependence of O3O2 on metallicity (e.g. Fig. 1, Kewley & Dopita 2002), as already mentioned in Sec. 1. Specifically, in the low-mass galaxy the highest metallicities (up to $12 + \log(O/H) \sim 8.8$) are found in several clumps all around the field of view. The high-mass galaxy, in contrast, displays higher metallicities (with values up to $12 + \log(O/H) \sim 9.1$) and an al-

most regular metallicity gradient, with some deviations only in the inter-arm regions. In this high-metallicity regime the O3O2 line ratio is only marginally sensitive to $\log(q)$ (Kewley & Dopita 2002), and thus the higher values of the O3O2 line ratio observed in the centre can be explained by the metallicity enhancement.

Interestingly, in these two galaxies the ionisation parameter does not show a monotonic and smooth radial profile, but, similarly to the S3S2 line ratio map, is enhanced in ‘structures’ which follow the $EW(H\alpha)$ maps, concentrated along the spiral arms visible in the $g - r - i$ images.

Finally, the gas extinction is low across the entire FoV of the lower-mass galaxy, with values below $E(B-V) \sim 0.1$, but shows a radial gradient in the high-mass galaxy, with values up to $E(B-V) \sim 0.5$ in the central regions.

4.2. The shape of the metallicity gradients

In the following, we analyse the radial profiles and gradients of metallicity, ionisation parameter and gas extinction for all the 1795 galaxies, keeping in mind that some of these quantities may have trends not well reproduced by a simple radial average, as shown in the example maps.

To determine the radial gradients, we used the deprojected distance of each spaxel derived by Belfiore et al. (2017), taking into account the inclination from the measured semi-axis ratio, assuming a constant oblateness of 0.13. Following the approach of Sánchez et al. (2014), Ho et al. (2015) and Belfiore et al. (2017), we adopt as a scale length to normalise the gradients the elliptical Petrosian effective radius (henceforth R_e), which is the most robust measure of the photometric properties of MaNGA galaxies provided by the NSA catalogue. The median radial profile of each quantity is computed for every galaxy in the range $0.5 - 2 R_e$ (in bins of 0.2 dex) as the median of the quantity measured in the spaxels lying in each bin. Then the median profiles are divided in eight bins of stellar mass, in the

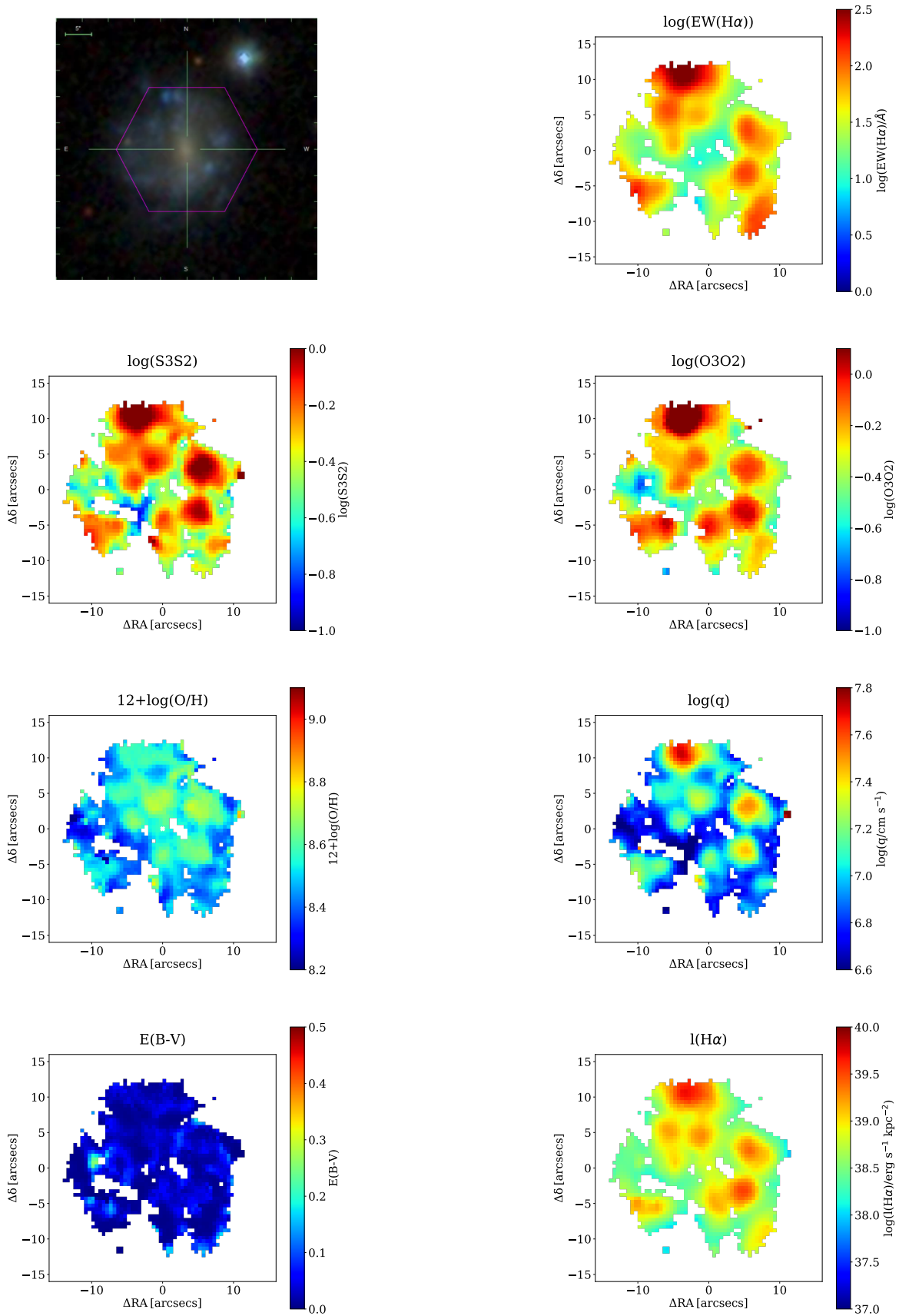


Fig. 10. Maps for the galaxy 8147-9102, with a stellar mass $\log(M_*/M_\odot) = 9.10$. The $g - r - i$ image composite from SDSS with the MaNGA hexagonal FoV overlaid, equivalent width of $H\alpha$, S3S2, O3O2, IZI metallicity $12+\log(O/H)$, IZI ionisation parameter $\log(q)$, IZI gas extinction $E(B-V)$ and $H\alpha$ luminosity per spaxel $L(H\alpha)$ maps are reported, respectively. East is to the left.

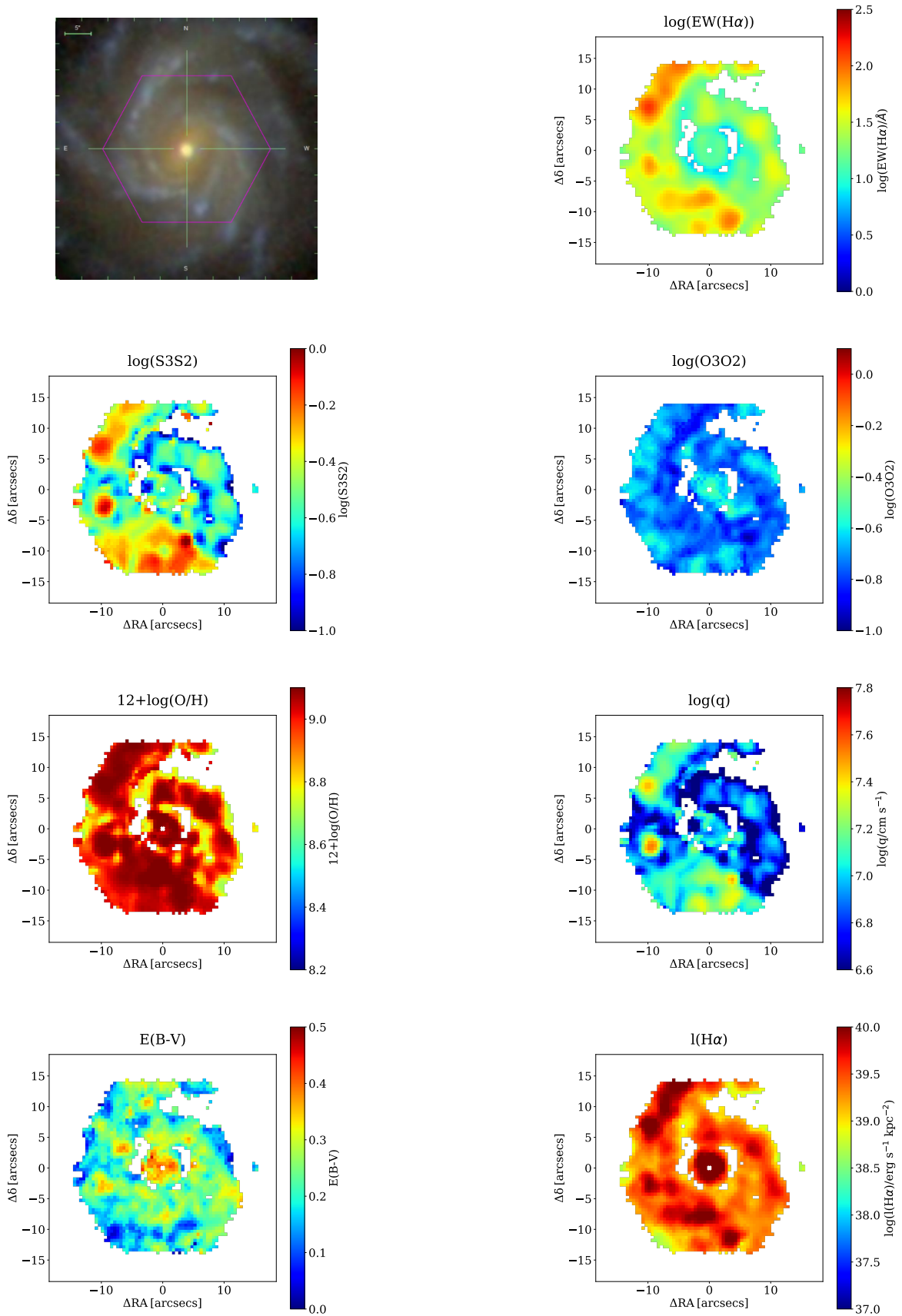


Fig. 11. Same as Fig. 10 for the galaxy 9041-12701, with a stellar mass $\log(M_{\star}/M_{\odot}) = 10.93$.

range $\log(M_*/M_\odot) = 9 - 11$ (in bins of 0.25 dex). The radial range is chosen to minimise the effects of inclination and beam-smearing on the metallicity gradients (Belfiore et al. 2017), and because of significant deviations from a linear fit are observed out of this range (Sánchez et al. 2014; Sánchez-Menguiano et al. 2016). The shaded regions in the following figures represent the 16th and 84th percentiles of the distribution in each stellar mass bin, divided by \sqrt{N} , where N is the number of galaxies lying in the bin. For each mass bin, a profile is computed only if more than 100 galaxies have a valid measured radial profile.

Fig. 12 displays the metallicity radial profiles computed with IZI for galaxies of different stellar mass (stellar mass bins as reported in the legend). The main observed features are the following:

- The mean oxygen abundance radial profiles are negative at all stellar masses in the range $[-0.05, -0.10]$ dex R_e^{-1} .
- The metallicity profile shape of galaxies with $\log(M_*/M_\odot) > 10.25$ is characterised by a flattening in the central regions ($R < 0.5 R_e$);
- Galaxies with $\log(M_*/M_\odot) < 10$ show a mild flattening of the radial metallicity profile in the outer regions ($R > 1.5 R_e$).
- The average slope shows a weak non-linear trend with stellar mass.

The negative abundance gradients are consistent with infall models of galaxy formation, that predict that spiral discs build up through accretion of material, which leads to an inside-out growth (Matteucci & Francois 1989; Molla et al. 1996; Boissier & Prantzos 1999; Belfiore et al. 2019). In this scenario, accretion brings gas into the inner regions of the discs, where high density leads to efficient star formation. The fast reprocessing of gas in the inner regions leads to a population of old, metal-rich stars in a high-metallicity gaseous environment. The outer regions, on the other hand, are characterised by younger, metal-poor stars surrounded by less enriched material (e.g., Davé et al. 2011; Gibson et al. 2013; Prantzos & Boissier 2000; Pilkington et al. 2012). The vertical offset between the different profiles is due to the mass-metallicity relation (Tremonti et al. 2004; Curti et al. 2019b).

A decrease or a nearly flat distribution of the abundance in the innermost region of discs was first observed by Belley & Roy (1992), while several works reported a flattening in the gradient in the outer regions (e.g. Martin & Roy 1995; Vilchez & Esteban 1996; Roy & Walsh 1997). This behaviour deviates from the pure inside-out scenario and could be due to the presence of radial migration (e.g. Minchev et al. 2011, 2012). Furthermore, the flattening of the metallicity gradient in the central region of the most massive spiral galaxies, found also in other works using CALIFA (e.g. Zinchenko et al. 2016) and MaNGA data (e.g. Belfiore et al. 2017), can be a consequence of the metallicity saturating in the central most metal rich regions and can readily be explained by classical inside-out chemical evolution models (Belfiore et al. 2019). One should also consider the possibility that contamination from the central LIER-like emission in massive galaxies may still contaminate the measured line fluxes (e.g., Maiolino & Mannucci 2019).

In Fig. 12, right panel, we show the metallicity profile slopes, estimated from a linear fit to the median profile in each mass bin, as red circles as a function of stellar mass. We observe a slight steepening with stellar mass in the range $\log(M_*/M_\odot) = 9 - 10.25$, going from -0.06 dex R_e^{-1} to -0.1 dex R_e^{-1} , and then a flattening down to -0.04 dex R_e^{-1} towards $\log(M_*/M_\odot) = 11$.

These mass trends may appear in contrast with the conclusions from Belfiore et al. (2017), who analysed gas-phase metal-

licity gradients using 550 star-forming MaNGA galaxies from a previous SDSS data release (data release 13). The metallicity gradients in Belfiore et al. (2017) are nearly flat for low-mass galaxies ($\log(M_*/M_\odot) = 9$) and become progressively steeper (more negative) for more massive galaxies until slopes ~ -0.15 dex R_e^{-1} at $\log(M_*/M_\odot) = 10.25$. A steepening of the metallicity gradient as a function of stellar mass - though weaker than the one observed by Belfiore et al. (2017) - is also inferred by Poetrodjojo et al. (2018), using data from the SAMI survey and an iterative process based on R23 and O3O2 to estimate $12+\log(\text{O}/\text{H})$ and $\log(q)$ (see Kobulnicky & Kewley 2004 for more details). This steepening is not per-se in contrast with the inside-out galaxy formation scenario (Belfiore et al. 2019), but may also point towards redistribution of metals in the early stages galaxy formation (see e.g. Maiolino & Mannucci 2019).

While the current sample of galaxies is larger than the one considered in Belfiore et al. (2017) and we make use of a different S/N selection criterion, the main discrepancy between the current work and Belfiore et al. (2017) is the method applied to infer metallicities. Indeed, in Belfiore et al. (2017) two strong-line ratio diagnostics were used, namely a calibration of R23 from Maiolino et al. (2008) (M08) and the well-established O3N2 calibration from Pettini & Pagel 2004 (PP04). To allow for a fairer comparison with Belfiore et al. (2017), in Fig. 12 we show the average metallicity gradients obtained applying the PP04 (blue squares) and M08 (green triangles) calibrations to the data presented in this work. The cyan dashed and the lime dotted lines are the results obtained by Belfiore et al. (2017) using PP04 and M08, respectively, and are fairly consistent with the gradients obtained with the current data set. At low stellar masses [$\log(M_*/M_\odot) < 9.75$], both the PP04 and M08 calibration find flatter gradients than IZI, in accordance to the findings in Belfiore et al. (2017). It is reassuring that some of the qualitative features (e.g. the flattening in the central regions of massive galaxies) are found for different choices of calibrator. It seems, moreover, that the slope of the metallicity gradients for low-mass galaxies was found to be too shallow in Belfiore et al. (2017). Further work may be warranted to better understand the chemical abundance distribution on the low-mass end, especially in light of recent work pointing out the diversity of metallicity gradients exhibited by low-mass star-forming galaxies (Bresolin 2019).

4.3. The ionisation parameter on resolved scales

The ionisation parameter changes within galaxies are still surprisingly poorly understood, despite the importance of determining q for correctly utilising ISM diagnostics. Dopita et al. (2006b) argued that in the local universe ionisation parameter gradually decreases with M_* (see also Brinchmann et al. 2008). Some studies presented a possible correlation between ionisation parameter and star formation rate (SFR, e.g. Dopita et al. 2014; Kaplan et al. 2016), while others argue for a better correlation with specific SFR ($\text{sSFR} = \text{SFR}/M_*$, e.g., Kewley et al. 2015; Bian et al. 2016; Kaasinen et al. 2018). On the other hand, Ho et al. (2015) investigated ~ 50 galaxies from the CALIFA survey, finding indications of a smooth increase in the ionisation parameter from their centres to the outskirts, which they interpret as a radial change in the properties of the ionising radiation. Kaplan et al. (2016), instead, analysed the ionisation parameter distribution in 8 nearby galaxies with the VENGA survey (Blanc et al. 2013), finding a peak in the central parts and regions of localised enhancements in the outer disc of their galaxies. Finally, Poetrodjojo et al. (2018), analysing 25 face-on star-forming spiral

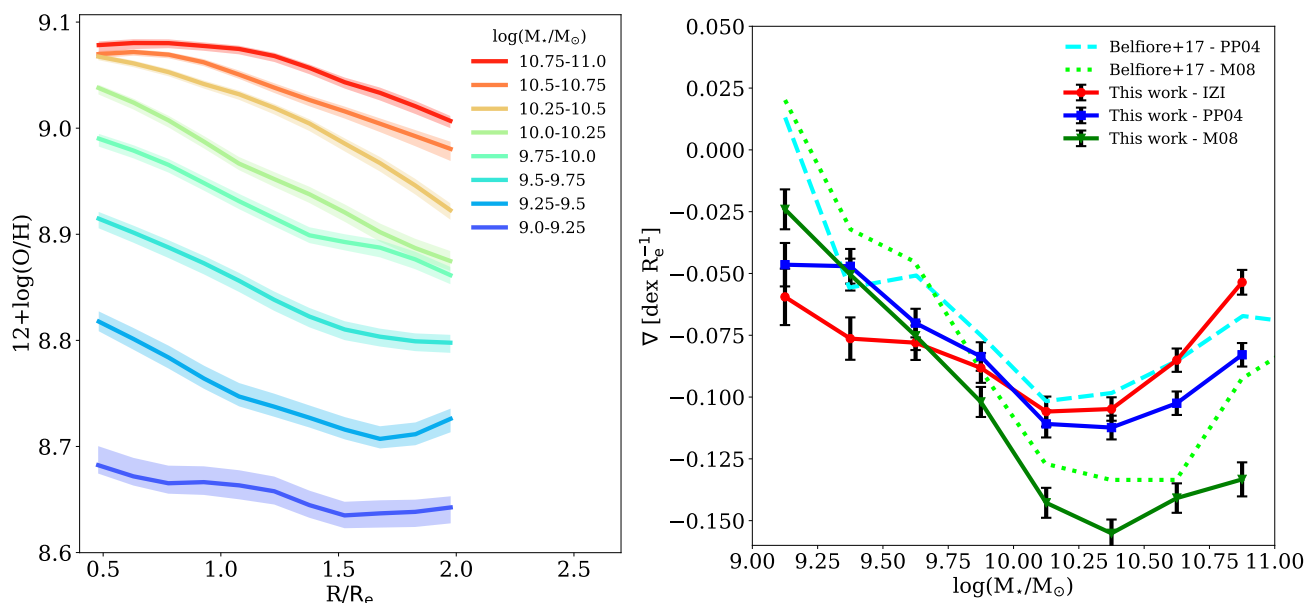


Fig. 12. *Left:* Oxygen abundance $12+\log(\text{O}/\text{H})$ as a function of the radius (in units of R_e), colour-coded as a function of the stellar mass $\log(M_*/M_\odot)$, as reported in the legend. The shaded regions represent the upper and lower errors of the radial gradients, obtained by calculating the 16th and 84th of the distribution in each stellar mass bin taking into account the number of galaxies lying in the bin. *Right:* Metallicity gradient estimated in the radial range 0.5–2 R_e from a linear fit of the corresponding radial profiles in different mass bins as a function of stellar mass (in red). The metallicity gradients estimated with M08 and PP04 calibrations are reported in green and blue, respectively, while those taken by Belfiore et al. (2017) are reported in lime and cyan.

galaxies from the SAMI survey, found that the ionisation parameter does not have clear radial or azimuthal trends, showing a range of different distributions ranging from weak gradients, to flat or clumpy distributions. All these authors estimated $\log(q)$ using the O3O2 diagnostic following the iterative method proposed by Kobulnicky & Kewley (2004), apart from Dopita et al. (2014), who used the method developed by Dopita et al. (2013), `pyqz`, that performs a two-dimensional fit to a given diagnostic grid, estimating metallicity and ionisation parameters for a given set of diagnostics

The left panel of Fig. 13 shows the radial profiles of ionisation parameter estimated by IZI, colour-coded as a function of stellar mass bins as reported in the legend. The right panel shows the slope of the radial profiles as a function of stellar mass. We highlight two main features from these figures:

- the ionisation parameter radial profiles are approximately flat at low stellar masses ($\log(M_*/M_\odot) < 10$), with slopes becoming more positive and steeper at increasing M_* , up to 0.15 dex R_e^{-1} at $\log(M_*/M_\odot) = 11$;
- in the central regions, galaxies of all masses show similar values of $\log(q)$ around $\log(q/\text{cm s}^{-1}) \sim 7.05 - 7.1$, while at large radii, higher stellar mass galaxies tend to have higher average values of $\log(q)$ (with values up to $\log(q/\text{cm s}^{-1}) \sim 7.3$).

The steepening with stellar mass and increasingly positive slopes of $\log(q)$ profiles echo the $EW(\text{H}\alpha)$ radial distributions as a function of stellar mass (see Fig. 3, Belfiore et al. 2018). These are found to be flat for low mass galaxies, becoming increasingly positive towards higher stellar masses. As discussed in Leitherer (2005), the equivalent width of the strongest hydrogen recombination lines, such as $EW(\text{H}\alpha)$, can be very powerful age indicators, measuring the ratio of the young, ionising stars over the old, non-ionising population (see also Kewley et al. 2015; Kaasinen et al. 2018). Therefore, $EW(\text{H}\alpha)$ is a good proxy for the sSFR, that is defined as the number of massive young (O,B) stars with

respect to the total number of formed stars. A similarity between $\log(q)$ and $EW(\text{H}\alpha)$ was already suggested by analysing Fig. 10 and Fig. 11.

In light of this, we investigated the dependence of the ionisation parameter on $EW(\text{H}\alpha)$, finding a strong correlation at all stellar masses, as shown in the left panel of Fig. 14, obtained dividing all the spaxels of each galaxy in $EW(\text{H}\alpha)$ bins of 0.15 dex, and then separating the galaxies in bins of stellar mass M_*/M_\odot , as reported in the legend. For $EW(\text{H}\alpha) > 14 \text{ \AA}$ (above the threshold of a possible DIG contamination; Lacerda et al. 2018), $\log(q)$ increases with $EW(\text{H}\alpha)$ following a nearly universal relation for galaxies of different masses. We quantify this relation with a linear slope in the log-log plane as

$$\log(q) = 0.56 \times \log(EW(\text{H}\alpha)) + 6.29 \quad (4)$$

with a scatter of 0.12 dex (dashed line in Fig. 14). This relation could be useful to constrain $\log(q)$ in order to calculate metallicity from a limited set of emission lines (e.g. $[\text{N II}]$ and $\text{H}\alpha$ in high- z galaxies). We also test the presence of a correlation between $\log(q)$ and $l(\text{H}\alpha)$. $l(\text{H}\alpha)$ traces the number of ionising photons produced by young and massive stars, and thus the current star formation on timescales of ~ 10 Myr (Calzetti et al. 2005, 2012). The right panel of Fig. 14 shows the ionisation parameter as a function of $l(\text{H}\alpha)$, dividing all the spaxels in this work in $l(\text{H}\alpha)$ bins of 0.15 dex, and then separating the galaxies in bins of stellar mass M_*/M_\odot . No universal relation is found between $\log(q)$ and $l(\text{H}\alpha)$. Indeed, $\log(q)$ increases with $l(\text{H}\alpha)$ at the lowest stellar masses ($M_*/M_\odot = 9$), while it decreases at the highest stellar masses ($M_*/M_\odot = 11$).

Interestingly, Pellegrini et al. (2019) found a good correlation between ionisation parameter and the age of the stellar population (i.e. with $EW(\text{H}\alpha)$), that they explain in terms of a correlation between q and the hardness of the spectrum, without finding any correlation between q and SFR, in agreement with our findings.

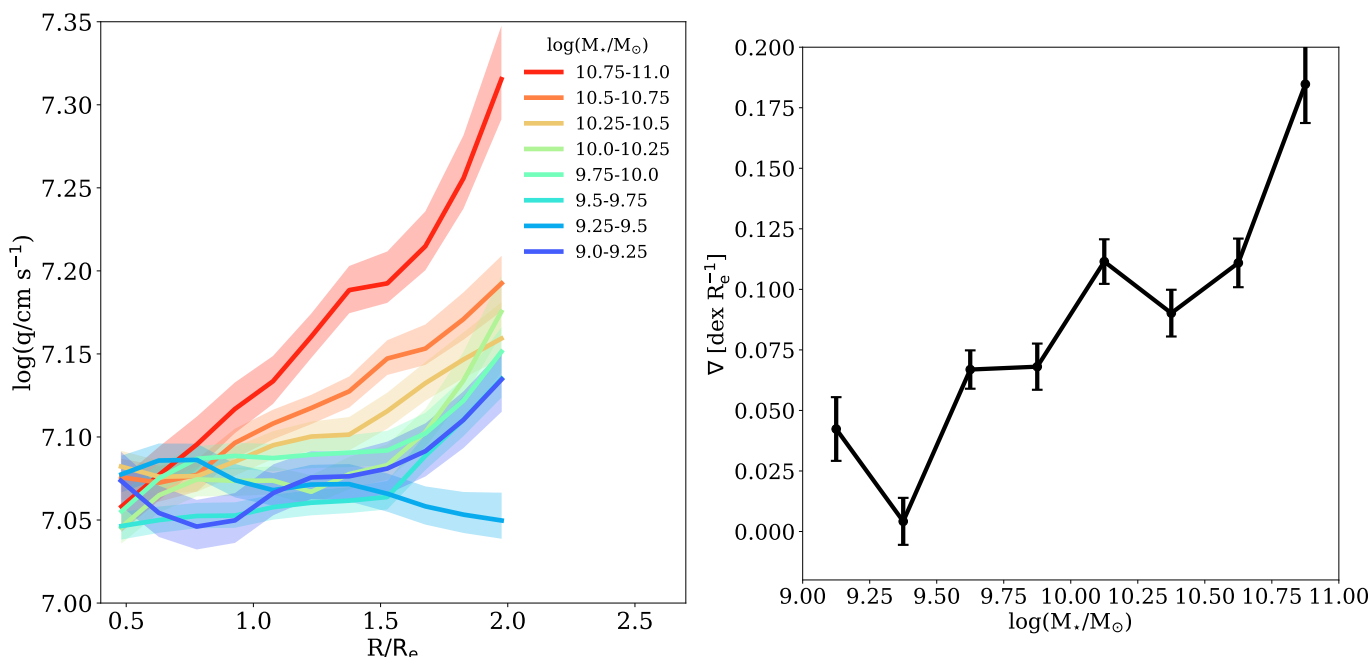


Fig. 13. *Left:* Ionisation parameter radial distribution (in units of R_e), colour-coded as a function of the stellar mass $\log(M_*/M_\odot)$, as reported in the legend. The shaded regions represent the 16th and 84th percentiles of the distribution in each stellar mass bin taking into account the number of galaxies lying in the bin. *Right:* $\log(q)$ radial profile slopes as a function of stellar mass in units of dex R_e^{-1} .

We note that, as evidenced in Fig. 13, the majority of spaxels have $\log(q)$ in the range $\log(q/\text{cm s}^{-1}) = 7.05 - 7.15$, while the correlation with $EW(H\alpha)$ observed in Fig. 14 only starts to appear for all masses for $\log(q) > 7.2$. This indicates that the correlation is driven by spaxels corresponding to the brightest H II regions. The flat $\log(q)$ radial profiles are the result of averaging a very clumpy distribution in $\log(q)$ with a large scatter, as highlighted in Fig. 10 and Fig. 11. Therefore, the radial averages used here to derive radial trends might not be ideal to understand the variations of q across the galaxy discs, that seem to be dominated by sSFR variations traced by $EW(H\alpha)$.

The left and right panels of Fig. 4.3 show $\log(S3S2)$ and $\log(O3O2)$ radial distributions in stellar mass bins, derived analogously to Fig. 13. These line ratios are both proxies for the ionisation parameter, and consistently show that low-mass galaxies are characterised by higher values of $\log(S3S2)$ and $\log(O3O2)$ and by flatter radial profiles. High-mass galaxies, on the other hand, tend to show positive slopes. Interestingly, we used S3S2 line ratios as a prior for $\log(q)$, so the $\log(q)$ radial distribution should closely follow the same trend. However, comparing the right panels of Fig. 13 and Fig. 4.3 the $\log(q)$ distribution obtained with IZI shows higher values for higher mass galaxies. On the one hand, this “flip” with stellar masses could be due to the residual dependence of these line ratios on metallicity. Up to $\log(q/\text{cm s}^{-1}) = 7.5$ (where the majority of spaxels lies) the $\log(q)$ values retrieved by IZI are slightly lower with respect to the prediction of Eq. 2, and the discrepancy depends on metallicity. Interestingly, this happens even though the input prior is not metallicity-dependent. IZI, however, will predict a metallicity dependence of the relation between $\log(S3S2)$ and ionisation parameter as a consequence of the information provided by the other emission lines. Above $\log(q/\text{cm s}^{-1}) = 7.5$, $\log(q)$ retrieved by IZI is fairly consistent with D91. This leads to a “re-calibrated” relation between $\log(S3S2)$ and $\log(q)$, highlighted by the magenta dotted line in Fig. 16 and given by

$$\log(S3S2) = 0.76 \times \log(q) - 5.70, \quad (5)$$

with a scatter of 0.11 dex, obtained using all the selected spaxels. On the other hand, this residual dependence of $\log(S3S2)$ on metallicity after adding a prior on the ionisation parameter could also point to the fact that IZI still suffers from a certain degree of degeneracy between the $12+\log(O/H)$ and $\log(q)$. Another possibility is that the difference between the $[S\text{ III}]/[S\text{ II}]$ derived value for q and the IZI output could be due to residual problems of the photoionisation models used in reproducing the observed line ratios. Therefore, a new generation of photoionisation models, designed to reproduce the sulfur emission lines as well, is required to better assess this issue.

Finally, Fig. 17 shows the relation between $EW(H\alpha)$ and ionisation parameter in bins of metallicity, obtained by IZI, indicating that at fixed $EW(H\alpha)$ there is a clear correlation between $\log(q)$ and $12+\log(O/H)$. However, this correlation disappears going towards the highest value of $EW(H\alpha)$ ($EW(H\alpha) > 150 \text{ \AA}$). A correlation between the two quantities is in contrast with the theoretical relation presented in Dopita & Evans (1986) and Dopita et al. (2006b) [$\log(q/\text{cm s}^{-1}) \propto 12+\log(O/H)^{-0.8}$]. However, Ho et al. (2015), Kaplan et al. (2016) and Poetrodjojo et al. (2018) do not find any clear radial trend between ionisation parameter and gas metallicity, both when considering regions at different galactocentric distances and in the 2-D maps, while Dopita et al. (2014) found a positive correlation between the two quantities. Dopita et al. (2014) explained the positive correlation between $12+\log(O/H)$ and $\log(q)$ as a consequence of the positive correlation that they find between SFR density and ionisation parameter. They conclude that the correlation between SFR density and $\log(q)$ is mainly caused by geometrical effects (i.e. overlapping between H II regions or non-spherical geometries), but is also due to the presence of dense gas in the vicinity of H II regions. On the other hand, Cresci et al. (2017) investigated the physical properties of the ionised gas in the prototypical H II galaxy He 2-10, finding that the central extreme star forming knots are highly enriched with super solar metallicity and characterised by a large ionisation parameter, highlighting again a correlation between the two quantities.

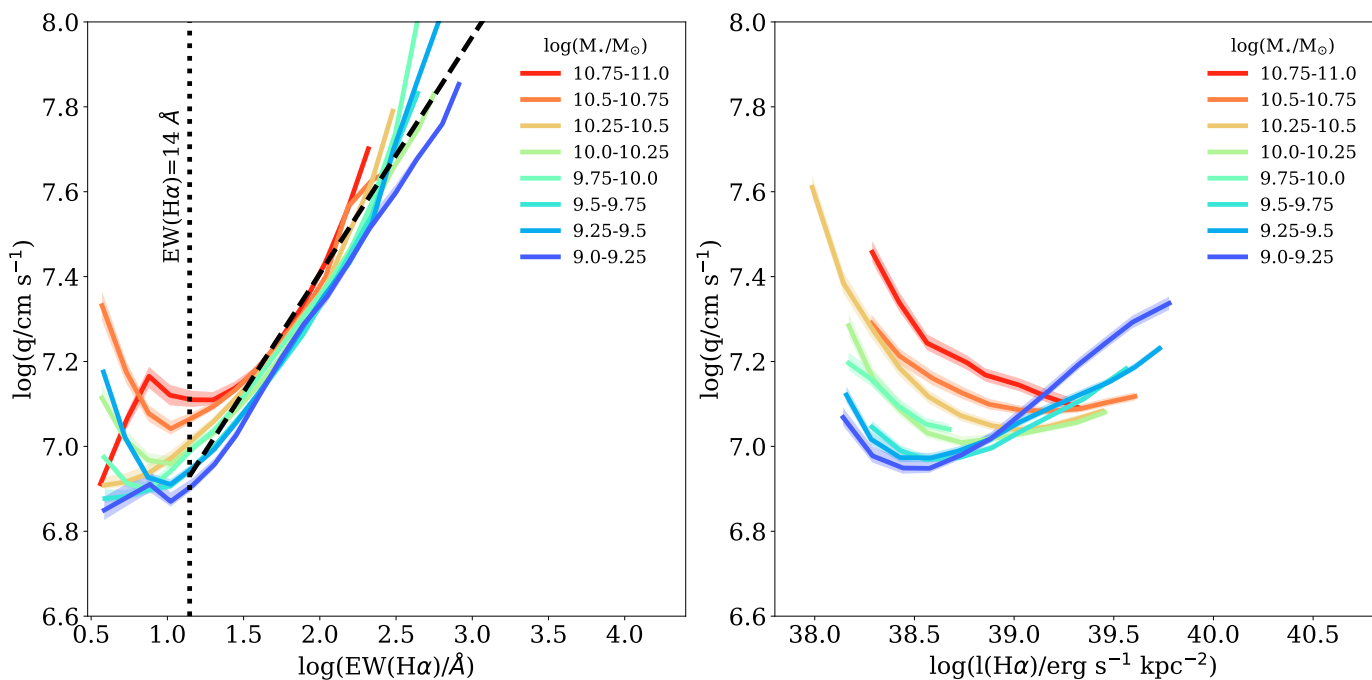


Fig. 14. *Left:* Ionisation parameter $\log(q)$ as a function of $H\alpha$ equivalent width [$EW(H\alpha)/\text{\AA}$] dividing all the spaxels used in this work in bins of 0.15 dex, and then separating the galaxies in bins of stellar mass, as reported in the legend. A nearly-universal power-law relation is evident between the two quantities for $EW(H\alpha) > 14 \text{ \AA}$ (labelled with a dotted vertical line). *Right:* Same as the left panel but for $H\alpha$ luminosity per spaxel [$l(H\alpha)/\text{erg s}^{-1}$]. No universal relation is found in this case.

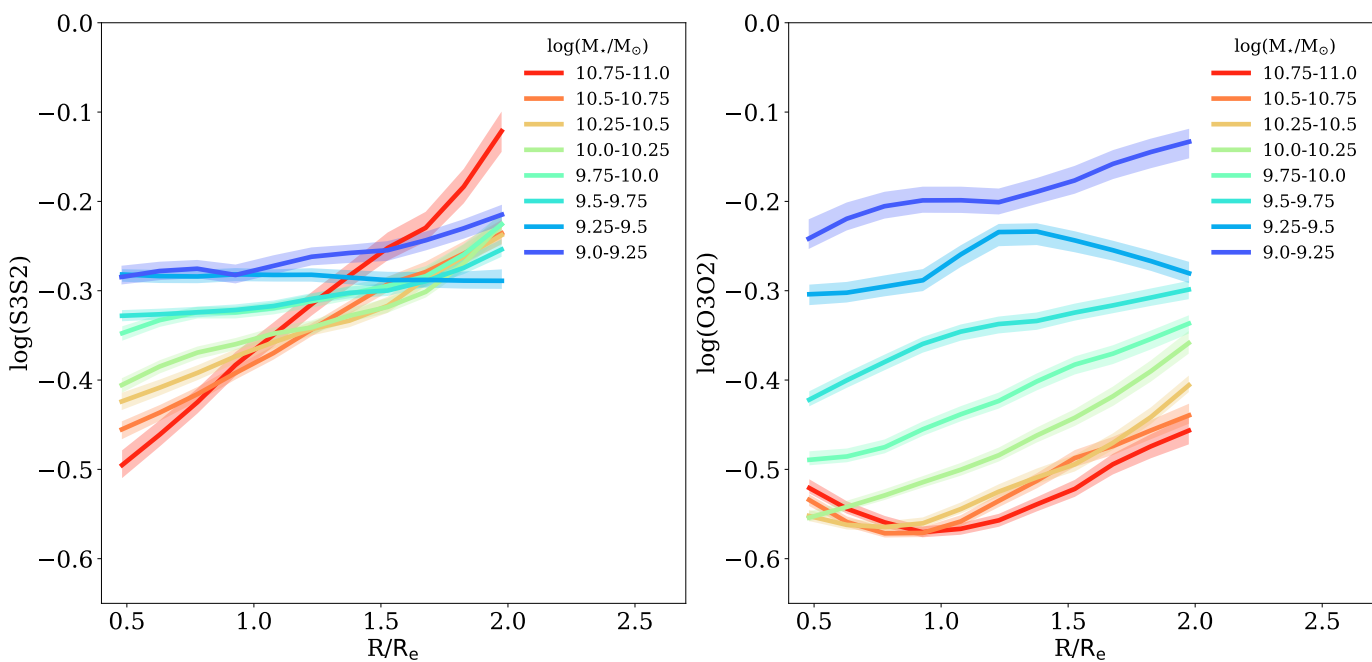


Fig. 15. S3S2 and O3O2 radial distributions, in bins of stellar mass M_*/M_\odot , as reported in the legend, respectively.

4.4. Gas extinction

The left panel of Fig. 18 illustrates the radial profiles of gas extinction $E(B-V)$ estimated by IZI, colour-coded as a function of stellar mass bins as reported in the legend, while the right panel shows the radial profile as a function of stellar mass. We report on these profiles only briefly in this work, since they will be the subject of future work by our team. Here we only highlight two main features of these figures:

- the $E(B-V)$ radial profiles show a strong dependence on stellar mass, with slopes around $-0.02 \text{ dex } R_e^{-1}$ at $\log(M_*/M_\odot) = 9$ and increasingly negative and steeper slopes in the range up to $\sim -0.13 \text{ dex } R_e^{-1}$ at larger stellar masses;
- $E(B-V) \sim 0.07$ for the lowest mass galaxies and reaches values as high as $E(B-V) \sim 0.4$ in the central regions of the more massive galaxies.

Indeed our findings in this section are not surprising, since more massive galaxies usually have larger dust reservoirs, espe-

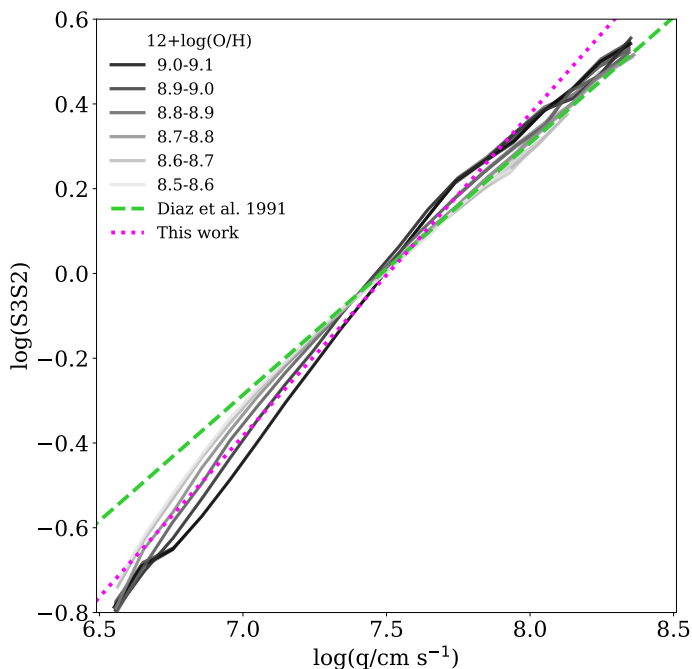


Fig. 16. Distribution of $\log(S3S2)$ as a function of $\log(q)$ inferred with IZI is shown in shades of grey, while its linear fit is given by the dotted magenta line. The green dashed line illustrates the D91 calibration, used as a prior.

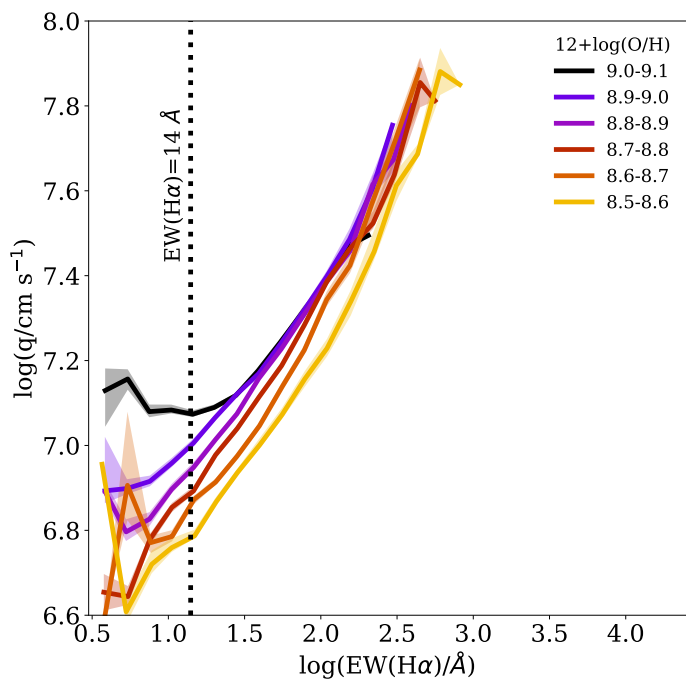


Fig. 17. Ionisation parameter $\log(q)$ as a function of $\log(EW(H\alpha))$ dividing all the spaxels used in this work in bins of 0.15 dex, and then separating the galaxies in bins of metallicity, as reported in the legend.

cially in the central regions (Bell & de Jong 2000). Since dust is formed from metals, a correlation between dust and the gas-phase oxygen abundance is expected and observed both in the local universe (e.g., Heckman et al. 1998; Zahid et al. 2013) and at high redshift (e.g., Reddy et al. 2010). A follow-up study of the relation between gas extinction and other galaxy properties will be presented in a forthcoming paper.

Fig. 19 shows the histogram of the difference between gas extinction obtained by assuming a fixed $H\alpha/H\beta$ line ratio of 2.86 and the one retrieved by IZI [$\Delta E(B-V)$]. The two quantities are pretty consistent, but in general IZI tends to retrieve slightly lower $E(B-V)$ values, in agreement with Brinchmann et al. (2004).

5. Conclusions

In this work we investigated the gas phase metallicity, ionisation parameter and gas extinction for a sample of 1795 local star forming galaxies, spanning the stellar mass range $10^9 - 10^{11} M_{\odot}$, by exploiting integral field spectroscopy from the SDSS-IV MaNGA DR 15. We selected star forming galaxies following the classification scheme proposed in Belfiore et al. (2016), further excluding spaxels which are not classified as star forming according to both the [N II]- and the [S II]-BPT diagrams. Moreover, we excluded spaxels with $S/N(H\alpha) < 15$, which assures that the main optical emission lines (i.e. [O II] $\lambda\lambda 3726, 29$, $H\beta$, [O III] $\lambda\lambda 4959, 5007$, [N II] $\lambda\lambda 6548, 84$, $H\alpha$, [S II] $\lambda\lambda 6717$, [S II] $\lambda\lambda 6731$ and [S III] $\lambda\lambda 9069, 9532$) are generally detected with $S/N > 1.5$ without introducing metallicity biases. We characterise self-consistently the gradients of metallicity, ionisation parameter and gas extinction with a method that consists in an update of the software tool IZI (Blanc et al. 2015), which compares an arbitrary set of observed emission lines with photoionisation model grids. Our revised version takes as input observed (as opposed to de-reddened) fluxes and simultaneously estimates the dust extinction ($E(B-V)$).

In the following we summarise our main findings.

- We confirm the existence of a discrepancy between models and observations of the [S III] lines already reported in the literature that persists with observations of a large sample of local galaxies and latest-generation photoionisation models (based on both the MAPPINGS and CLOUDY codes) (Fig. 3).
- We argue that the set of emission lines comprising [O II] $\lambda\lambda 3726, 29$, $H\beta$, [O III] $\lambda\lambda 4959, 5007$, [N II] $\lambda\lambda 6548, 84$, $H\alpha$, [S II] $\lambda\lambda 6717$ and [S II] $\lambda\lambda 6731$ is not sufficient to break the degeneracy between metallicity and ionisation parameter with the current photoionisation models. We therefore used the [S III] lines to add extra information to the fit performed with our revised version of IZI, taking into account a Gaussian prior based on the D91 calibration, that links S3S2 to q (Sec. 3.4).
- The oxygen abundance radial profiles (in the range $0.5-2 R_e$) have negative slopes [$-0.1 \text{ dex } R_e^{-1}$ to $-0.04 \text{ dex } R_e^{-1}$], and show a flattening in more massive systems. Galaxies with $\log(M_{\star}/M_{\odot}) > 10.25$ show a flat gradient in the central regions ($R \sim 0.5 R_e$), while galaxies with $\log(M_{\star}/M_{\odot}) < 10$ tend to have a flatter gradients in the external regions ($R > 1.5 R_e$) (Fig. 12).
- The ionisation parameter gradients are approximately flat at low stellar masses ($\log(M_{\star}/M_{\odot}) < 10$), and tend to steepen (more positive slopes) at increasing M_{\star} . In galaxy outskirts, higher stellar mass galaxies tend to have higher average values of $\log(q)$ than less massive objects. All galaxies, however, show a median value around $\log(q) \sim 7.05 - 7.1$ in the central regions (Fig. 13).
- A tight correlation between $\log(EW(H\alpha))$ and $\log(q)$ is observed at all stellar masses, expressed by a simple power-law relation for $EW(H\alpha) > 14 \text{ \AA}$. A clear correlation between $l(H\alpha)$ (i.e. SFR) and $\log(q)$ is only found in low-mass galaxies, but this correlation does not hold for the whole galaxy sample (Fig. 14).

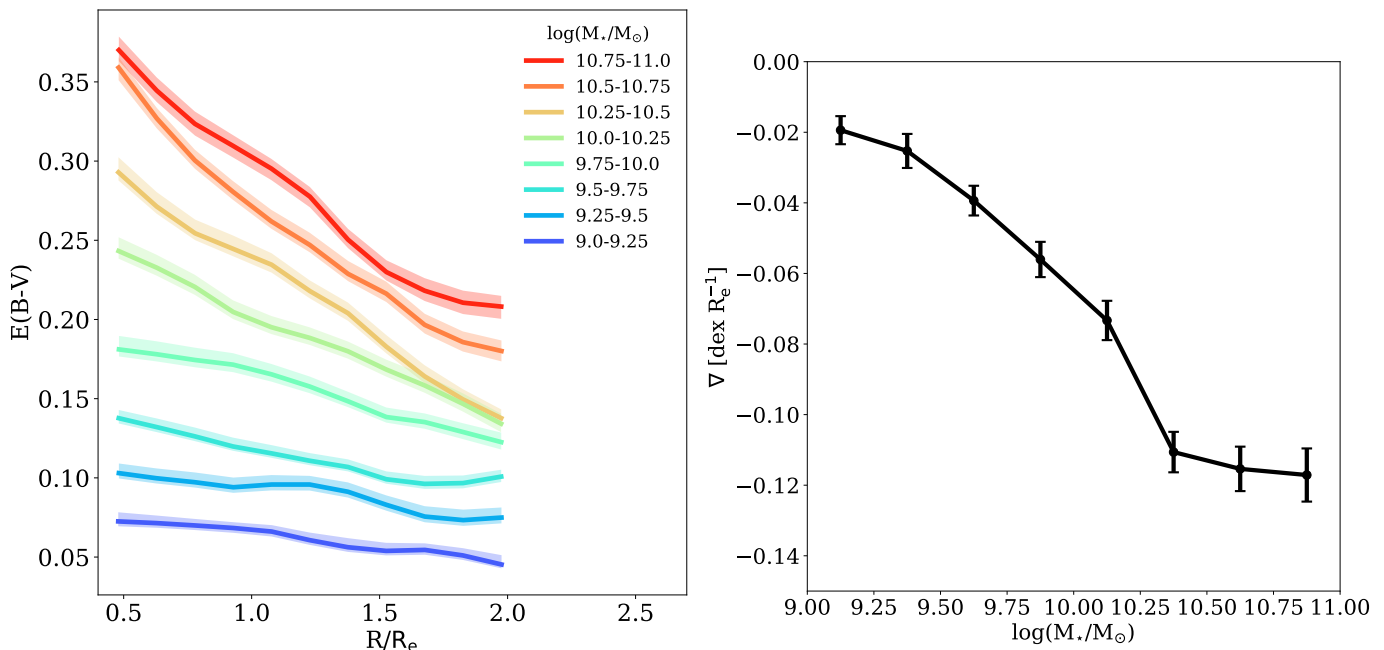


Fig. 18. *Left:* Gas extinction radial distribution (in units of R_e), colour-coded as a function of the stellar mass $\log(M_*/M_\odot)$, as reported in the legend. The shaded regions represent the 16th and 84th percentiles of the distribution in each stellar mass bin taking into account the number of galaxies lying in the bin. *Right:* Slope of the radial profiles of $E(B-V)$ in units of mag/R_e as a function of stellar mass.

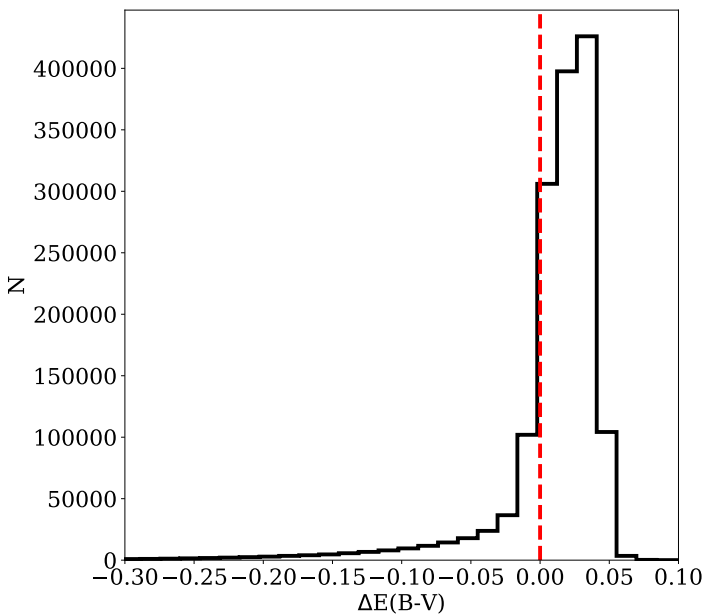


Fig. 19. Histogram of the difference between the $E(B-V)$ obtained by assuming a fixed $H\alpha/H\alpha$ line ratio of 2.86 and the one retrieved by IZI.

- A correlation between metallicity and ionisation parameter is found at fixed $EW(H\alpha)$ up to $EW(H\alpha) < 150$ (Fig. 17).
- The gas extinction radial gradients strongly depend on stellar mass. $E(B-V)$ slopes are approximately flat at $\log(M_*/M_\odot) = 9$ with values of $E(B-V) \sim 0.07$ mag. The profiles steepen towards higher stellar masses, and $E(B-V)$ reaches values as high as ~ 0.4 mag in the central regions of the more massive systems (Fig. 18).

The work presented in this paper can be seen as a first step in the simultaneous study of $12+\log(O/H)$ and q within a large set of galaxies. As such, it is affected by some limitations. For exam-

ple, at this stage we have not included in our analysis the variation of N/O ratio and the effective temperature of the stellar cluster. Indeed, the nucleosynthetic origin of nitrogen is more complex than that of oxygen, and its nucleosynthesis is metallicity-dependent, implying a non-linear relation between O/H and N/O (see e.g. Belfiore et al. 2017; Schaefer et al. 2019). Furthermore, the effective temperature of the exciting stars is related to both metallicity and ionisation parameter since it increases as metallicity is lowered, but the mechanical energy flux in the stellar winds decreases towards lower metallicity, causing changes in the ionisation parameter (see e.g. Pérez-Montero & Díaz 2005; Dopita et al. 2006b,a; Pérez-Montero 2014). Since these fundamental parameters of H II regions are not independent, more physical H II region models, such as WARPFIELD-EMP (Rahner et al. 2017; Pellegrini et al. 2019), that allows to model the time evolution of feedback in molecular clouds taking into account the physical processes regulating the emission from the clouds (e.g. stellar winds, radiation, supernovae, gravity, thermal conduction, cooling), may be helpful in reducing the size of the parameter space to be explored.

However, the main drawback of the current approach lies in the limitations of the current photoionisation models. Even though the model grids are generally able to reproduce the bulk properties of H II regions in galaxies, we have shown here that S3S2 is not well reproduced by any of the state-of-the-art model grids taken into account in this work. This fact severely limits the usefulness of S3S2 at present as a tracer of the ionisation parameter.

Acknowledgements

We thank Nell Byler for sharing her CLOUDY models and for assistance with their use, and Kathryn Kreckel for sharing the PHANGS data shown in this work. We thank Sebastian Sanchez for support on the Pipe3D Value-Added Catalog for MaNGA DR15. We are grateful to Mike Dopita and Emily Levesque for making their photoionisation model grids publicly available. We acknowledge F. Mannucci for his

precious advice and the anonymous referee for their comments and suggestions, which contributed to improve the quality of our work. MM and GC have been supported by the INAF PRIN-SKA 2017 programme 1.05.01.88.04. MB acknowledges FONDECYT regular grant 1170618. RM acknowledges ERC Advanced Grant 695671 "QUENCH" and support by the Science and Technology Facilities Council (STFC).

This work makes use of data from SDSS-IV. Funding for the Sloan Digital Sky Survey IV has been provided by the Alfred P. Sloan Foundation, the U.S. Department of Energy Office of Science, and the Participating Institutions. SDSS acknowledges support and resources from the Center for High-Performance Computing at the University of Utah. The SDSS web site is www.sdss.org. This research made use of Marvin, a core Python package and web framework for MaNGA data, developed by Brian Cherinka, José Sánchez-Gallego, and Brett Andrews (Cherinka et al. 2018). SDSS is managed by the Astrophysical Research Consortium for the Participating Institutions of the SDSS Collaboration including the Brazilian Participation Group, the Carnegie Institution for Science, Carnegie Mellon University, the Chilean Participation Group, the French Participation Group, Harvard-Smithsonian Center for Astrophysics, Instituto de Astrofísica de Canarias, The Johns Hopkins University, Kavli Institute for the Physics and Mathematics of the Universe (IPMU) / University of Tokyo, the Korean Participation Group, Lawrence Berkeley National Laboratory, Leibniz Institut für Astrophysik Potsdam (AIP), Max-Planck-Institut für Astronomie (MPIA Heidelberg), Max-Planck-Institut für Astrophysik (MPA Garching), Max-Planck-Institut für Extraterrestrische Physik (MPE), National Astronomical Observatories of China, New Mexico State University, New York University, University of Notre Dame, Observatório Nacional / MCTI, The Ohio State University, Pennsylvania State University, Shanghai Astronomical Observatory, United Kingdom Participation Group, Universidad Nacional Autónoma de México, University of Arizona, University of Colorado Boulder, University of Oxford, University of Portsmouth, University of Utah, University of Virginia, University of Washington, University of Wisconsin, Vanderbilt University, and Yale University. The MaNGA data used in this work is publicly available at <http://www.sdss.org/dr15/manga/manga-data/>.

References

- Aguado, D. S., Ahumada, R., Almeida, A., et al. 2019, *ApJS*, 240, 23
 Ali, B., Blum, R. D., Bumgardner, T. E., et al. 1991, *PASP*, 103, 1182
 Alloin, D., Collin-Souffrin, S., Joly, M., & Vigroux, L. 1979, *A&A*, 78, 200
 Anders, E. & Grevesse, N. 1989, *Geochim. Cosmochim. Acta*, 53, 197
 Andrews, B. H. & Martini, P. 2013, *ApJ*, 765, 140
 Asplund, M., Grevesse, N., Sauval, A. J., & Scott, P. 2009, *ARA&A*, 47, 481
 Azimlu, M., Marciniak, R., & Barmby, P. 2011, *AJ*, 142, 139
 Baldwin, J. A., Phillips, M. M., & Terlevich, R. 1981, *PASP*, 93, 5
 Belfiore, F., Maiolino, R., Bundy, K., et al. 2018, *MNRAS*, 477, 3014
 Belfiore, F., Maiolino, R., Maraston, C., et al. 2016, *MNRAS*, 461, 3111
 Belfiore, F., Maiolino, R., Tremonti, C., et al. 2017, *MNRAS*, 469, 151
 Belfiore, F., Vincenzo, F., Maiolino, R., & Matteucci, F. 2019, *MNRAS*, 487, 456
 Belfiore, F., Westfall, K. B., Schaefer, A., et al. 2019, arXiv e-prints, arXiv:1901.00866
 Bell, E. F. & de Jong, R. S. 2000, *MNRAS*, 312, 497
 Belley, J. & Roy, J.-R. 1992, *ApJS*, 78, 61
 Bian, F., Kewley, L. J., Dopita, M. A., & Juneau, S. 2016, *ApJ*, 822, 62
 Blanc, G. A., Kewley, L., Vogt, F. P. A., & Dopita, M. A. 2015, *ApJ*, 798, 99
 Blanc, G. A., Lu, Y., Benson, A., Katsianis, A., & Barraza, M. 2019, *ApJ*, 877, 6
 Blanc, G. A., Weinzirl, T., Song, M., et al. 2013, *AJ*, 145, 138
 Blanton, M. R., Bershady, M. A., Abolfathi, B., et al. 2017, *AJ*, 154, 28
 Blanton, M. R., Kazin, E., Muna, D., Weaver, B. A., & Price-Whelan, A. 2011, *AJ*, 142, 31
 Boissier, S. & Prantzos, N. 1999, *MNRAS*, 307, 857
 Bresolin, F. 2019, *MNRAS*, 488, 3826
 Brinchmann, J., Charlot, S., White, S. D. M., et al. 2004, *MNRAS*, 351, 1151
 Brinchmann, J., Pettini, M., & Charlot, S. 2008, *MNRAS*, 385, 769
 Bundy, K., Bershady, M. A., Law, D. R., et al. 2015, *ApJ*, 798, 7
 Byler, N., Dalcanton, J. J., Conroy, C., & Johnson, B. D. 2017, *ApJ*, 840, 44
 Calzetti, D. 1997, *AJ*, 113, 162
 Calzetti, D., Armus, L., Bohlin, R. C., et al. 2000, *ApJ*, 533, 682
 Calzetti, D., Kennicutt, R. C., J., Bianchi, L., et al. 2005, *ApJ*, 633, 871
 Calzetti, D., Liu, G., & Koda, J. 2012, *ApJ*, 752, 98
 Cappellari, M., McDermid, R. M., Alatalo, K., et al. 2013, *MNRAS*, 432, 1862
 Charlot, S. & Longhetti, M. 2001, *MNRAS*, 323, 887
 Cherinka, B., Andrews, B. H., Sánchez-Gallego, J., et al. 2018, arXiv e-prints [arXiv:1812.03833]
 Choi, J., Dotter, A., Conroy, C., et al. 2016, *ApJ*, 823, 102
 Conroy, C., Gunn, J. E., & White, M. 2009, *ApJ*, 699, 486
 Cresci, G., Vanzì, L., Telles, E., et al. 2017, *A&A*, 604, A101
 Curti, M., Cresci, G., Mannucci, F., et al. 2017, *MNRAS*, 465, 1384
 Curti, M., Maiolino, R., Cirasuolo, M., et al. 2019a, arXiv e-prints, arXiv:1910.13451
 Curti, M., Mannucci, F., Cresci, G., & Maiolino, R. 2019b, arXiv e-prints, arXiv:1910.00597
 D'Agostino, J. J., Kewley, L. J., Groves, B., et al. 2019, *The Astrophysical Journal*, 878, 2
 Davé, R., Finlator, K., & Oppenheimer, B. D. 2011, *MNRAS*, 416, 1354
 Denicoló, G., Terlevich, R., & Terlevich, E. 2002, *MNRAS*, 330, 69
 Díaz, A. I. & Pérez-Montero, E. 2000, *MNRAS*, 312, 130
 Díaz, A. I., Terlevich, E., Vilchez, J. M., Pagel, B. E. J., & Edmunds, M. G. 1991, *MNRAS*, 253, 245
 Dinerstein, H. L. & Shields, G. A. 1986, *ApJ*, 311, 45
 Dopita, M. A. & Evans, I. N. 1986, *ApJ*, 307, 431
 Dopita, M. A., Fischera, J., Sutherland, R. S., et al. 2006a, *The Astrophysical Journal Supplement Series*, 167, 177
 Dopita, M. A., Fischera, J., Sutherland, R. S., et al. 2006b, *ApJ*, 647, 244
 Dopita, M. A., Groves, B. A., Fischera, J., et al. 2005, *ApJ*, 619, 755
 Dopita, M. A., Groves, B. A., Sutherland, R. S., & Kewley, L. J. 2003, *ApJ*, 583, 727
 Dopita, M. A., Kewley, L. J., Heisler, C. A., & Sutherland, R. S. 2000, *ApJ*, 542, 224
 Dopita, M. A., Rich, J., Vogt, F. P. A., et al. 2014, *Ap&SS*, 350, 741
 Dopita, M. A., Sutherland, R. S., Nicholls, D. C., Kewley, L. J., & Vogt, F. P. A. 2013, *ApJS*, 208, 10
 Dotter, A. 2016, *ApJS*, 222, 8
 Draine, B. T. & Kraich, C. D. 2018, *ApJ*, 862, 30
 Drory, N., MacDonald, N., Bershady, M. A., et al. 2015, *AJ*, 149, 77
 Falcón-Barroso, J., Sánchez-Blázquez, P., Vazdekis, A., et al. 2011, *A&A*, 532, A95
 Ferland, G. J., Porter, R. L., van Hoof, P. A. M., et al. 2013, *Rev. Mexicana Astron. Astrofis.*, 49, 137
 Foreman-Mackey, D., Hogg, D. W., Lang, D., & Goodman, J. 2013, *PASP*, 125, 306
 Garnett, D. R. 1989, *ApJ*, 345, 282
 Gibson, B. K., Pilkington, K., Brook, C. B., Stinson, G. S., & Bailin, J. 2013, *A&A*, 554, A47
 Gunn, J. E., Siegmund, W. A., Mannery, E. J., et al. 2006, *AJ*, 131, 2332
 Gutiérrez, L., Beckman, J. E., & Buenrostro, V. 2011, *AJ*, 141, 113
 Heckman, T. M., Robert, C., Leitherer, C., Garnett, D. R., & van der Rydt, F. 1998, *ApJ*, 503, 646
 Hillier, D. J. & Miller, D. L. 1998, *ApJ*, 496, 407
 Ho, I. T., Kudritzki, R.-P., Kewley, L. J., et al. 2015, *MNRAS*, 448, 2030
 Hoopes, C. G. & Walterbos, R. A. M. 2003, *ApJ*, 586, 902
 Jones, T., Martin, C., & Cooper, M. C. 2015, *ApJ*, 813, 126
 Kaasinen, M., Kewley, L., Bian, F., et al. 2018, *MNRAS*, 477, 5568
 Kaplan, K. F., Jøgee, S., Kewley, L., et al. 2016, *MNRAS*, 462, 1642
 Kauffmann, G., Heckman, T. M., Tremonti, C., et al. 2003, *MNRAS*, 346, 1055
 Kehrig, C., Vilchez, J. M., Telles, E., Cuisinier, F., & Pérez-Montero, E. 2006, *A&A*, 457, 477
 Kewley, L. J. & Dopita, M. A. 2002, *ApJS*, 142, 35
 Kewley, L. J., Dopita, M. A., Sutherland, R. S., Heisler, C. A., & Trevena, J. 2001, *ApJ*, 556, 121
 Kewley, L. J. & Ellison, S. L. 2008, *ApJ*, 681, 1183
 Kewley, L. J., Groves, B., Kauffmann, G., & Heckman, T. 2006, *MNRAS*, 372, 961
 Kewley, L. J., Nicholls, D. C., & Sutherland, R. S. 2019, *ARA&A*, 57, 511
 Kewley, L. J., Zahid, H. J., Geller, M. J., et al. 2015, *ApJ*, 812, L20
 Kobulnicky, H. A. & Kewley, L. J. 2004, *ApJ*, 617, 240
 Kreckel, K., Ho, I. T., Blanc, G. A., et al. 2019, arXiv e-prints, arXiv:1910.07190
 Krühler, T., Kuncarayakti, H., Schady, P., et al. 2017, *A&A*, 602, A85
 Lacerda, E. A. D., Cid Fernandes, R., Couto, G. S., et al. 2018, *MNRAS*, 474, 3727
 Law, D. R., Cherinka, B., Yan, R., et al. 2016, *AJ*, 152, 83
 Law, D. R., Yan, R., Bershady, M. A., et al. 2015, *AJ*, 150, 19
 Leitherer, C. 2005, in *American Institute of Physics Conference Series*, Vol. 783, *The Evolution of Starbursts*, ed. S. Hüttmeister, E. Manthey, D. Bomans, & K. Weis, 280–295
 Leitherer, C., Schaerer, D., Goldader, J. D., et al. 1999, *ApJS*, 123, 3
 Lejeune, T., Cuisinier, F., & Buser, R. 1997, *A&AS*, 125
 Lequeux, J., Peimbert, M., Rayo, J. F., Serrano, A., & Torres-Peimbert, S. 1979, *A&A*, 500, 145
 Levesque, E. M., Kewley, L. J., & Larson, K. L. 2010, *AJ*, 139, 712

- Lilly, S. J., Carollo, C. M., Pipino, A., Renzini, A., & Peng, Y. 2013, *ApJ*, 772, 119
- Luridiana, V., Morisset, C., & Shaw, R. A. 2015, *A&A*, 573, A42
- Maiolino, R. & Mannucci, F. 2019, *A&A Rev.*, 27, 3
- Maiolino, R., Nagao, T., Grazian, A., et al. 2008, *A&A*, 488, 463
- Mannucci, F., Cresci, G., Maiolino, R., Marconi, A., & Gnerucci, A. 2010, *MNRAS*, 408, 2115
- Marino, R. A., Rosales-Ortega, F. F., Sánchez, S. F., et al. 2013, *A&A*, 559, A114
- Markwardt, C. B. 2009, in *Astronomical Society of the Pacific Conference Series*, Vol. 411, *Astronomical Data Analysis Software and Systems XVIII*, ed. D. A. Bohlender, D. Durand, & P. Dowler, 251
- Martin, P. & Roy, J.-R. 1995, *ApJ*, 445, 161
- Mathis, J. S. 1982, *ApJ*, 261, 195
- Mathis, J. S. 1985, *ApJ*, 291, 247
- Mathis, J. S., Rumpl, W., & Nordsieck, K. H. 1977, *ApJ*, 217, 425
- Matteucci, F. & Franco, P. 1989, *MNRAS*, 239, 885
- Minchev, I., Famaey, B., Combes, F., et al. 2011, *A&A*, 527, A147
- Minchev, I., Famaey, B., Quillen, A. C., et al. 2012, *A&A*, 548, A126
- Mingozzi, M., Cresci, G., Venturi, G., et al. 2019, *A&A*, 622, A146
- Mollá, M., Ferrini, F., & Diaz, A. I. 1996, *ApJ*, 466, 668
- Mollá, M., García-Vargas, M. L., & Bressan, A. 2009, *MNRAS*, 398, 451
- Morisset, C., Delgado-Inglada, G., Sánchez, S. F., et al. 2016, *A&A*, 594, A37
- Nicholls, D. C., Dopita, M. A., Sutherland, R. S., Kewley, L. J., & Palay, E. 2013, *ApJS*, 207, 21
- O'Donnell, J. E. 1994, *ApJ*, 422, 158
- Oey, M. S., Meurer, G. R., Yelda, S., et al. 2007, *ApJ*, 661, 801
- Osterbrock, D. E. 1989, *Astrophysics of gaseous nebulae and active galactic nuclei*
- Osterbrock, D. E. & Ferland, G. J. 2006, *Mercury*, 35, 40
- Pagel, B. E. J., Edmunds, M. G., Blackwell, D. E., Chun, M. S., & Smith, G. 1979, *MNRAS*, 189, 95
- Pauldrach, A. W. A., Hoffmann, T. L., & Lennon, M. 2001, *A&A*, 375, 161
- Pellegrini, E. W., Rahner, D., Reissl, S., et al. 2019, *arXiv e-prints*, arXiv:1909.09651
- Pérez-Montero, E. 2014, *MNRAS*, 441, 2663
- Pérez-Montero, E. & Díaz, A. I. 2005, *MNRAS*, 361, 1063
- Pettini, M. & Pagel, B. E. J. 2004, *MNRAS*, 348, L59
- Pilkington, K., Few, C. G., Gibson, B. K., et al. 2012, *A&A*, 540, A56
- Pilyugin, L. S. & Mattsson, L. 2011, *MNRAS*, 412, 1145
- Pilyugin, L. S. & Thuan, T. X. 2005, *ApJ*, 631, 231
- Pilyugin, L. S., Vílchez, J. M., Mattsson, L., & Thuan, T. X. 2012, *MNRAS*, 421, 1624
- Poetrodjojo, H., Groves, B., Kewley, L. J., et al. 2018, *MNRAS*, 479, 5235
- Prantzos, N. & Boissier, S. 2000, *MNRAS*, 313, 338
- Rahner, D., Pellegrini, E. W., Glover, S. C. O., & Klessen, R. S. 2017, *MNRAS*, 470, 4453
- Reddy, N. A., Erb, D. K., Pettini, M., Steidel, C. C., & Shapley, A. E. 2010, *ApJ*, 712, 1070
- Roy, J. R. & Walsh, J. R. 1997, *MNRAS*, 288, 715
- Sánchez, S. F., Avila-Reese, V., Hernandez-Toledo, H., et al. 2018, *Rev. Mexicana Astron. Astrofis.*, 54, 217
- Sánchez, S. F., Pérez, E., Sánchez-Blázquez, P., et al. 2016, *Rev. Mexicana Astron. Astrofis.*, 52, 171
- Sánchez, S. F., Rosales-Ortega, F. F., Iglesias-Páramo, J., et al. 2014, *A&A*, 563, A49
- Sánchez-Blázquez, P., Peletier, R. F., Jiménez-Vicente, J., et al. 2006, *MNRAS*, 371, 703
- Sánchez-Menguiano, L., Sánchez, S. F., Pérez, I., et al. 2016, *A&A*, 587, A70
- Sanders, R. L., Jones, T., Shapley, A. E., et al. 2019, *arXiv e-prints*, arXiv:1910.13594
- Sanders, R. L., Shapley, A. E., Kriek, M., et al. 2016, *ApJ*, 825, L23
- Sanders, R. L., Shapley, A. E., Zhang, K., & Yan, R. 2017, *ApJ*, 850, 136
- Schaefer, A. L., Tremont, C., Belfiore, F., et al. 2019, *arXiv e-prints*, arXiv:1911.00581
- Schaller, G., Schaerer, D., Meynet, G., & Maeder, A. 1992, *A&AS*, 96, 269
- Schlegel, D. J., Finkbeiner, D. P., & Davis, M. 1998, *ApJ*, 500, 525
- Schmutz, W., Leitherer, C., & Gruenwald, R. 1992, *PASP*, 104, 1164
- Smee, S. A., Gunn, J. E., Uomoto, A., et al. 2013, *AJ*, 146, 32
- Stasińska, G. 2004, in *Cosmochemistry. The melting pot of the elements*, ed. C. Esteban, R. García López, A. Herrero, & F. Sánchez, 115–170
- Stasińska, G. 2005, *A&A*, 434, 507
- Stasińska, G. 2006, *A&A*, 454, L127
- Stasińska, G., Vale Asari, N., Cid Fernandes, R., et al. 2008, *MNRAS*, 391, L29
- Storchi-Bergmann, T., Calzetti, D., & Kinney, A. L. 1994, *ApJ*, 429, 572
- Tremonti, C. A., Heckman, T. M., Kauffmann, G., et al. 2004, *ApJ*, 613, 898
- Vale Asari, N., Couto, G. S., Cid Fernandes, R., et al. 2019, *MNRAS*, 489, 4721
- Vazdekis, A., Ricciardelli, E., Cenarro, A. J., et al. 2012, *MNRAS*, 424, 157
- Vázquez, G. A. & Leitherer, C. 2005, *ApJ*, 621, 695
- Veilleux, S. & Osterbrock, D. E. 1987, *ApJS*, 63, 295
- Vílchez, J. M. & Esteban, C. 1996, *MNRAS*, 280, 720
- Wake, D. A., Bundy, K., Diamond-Stanic, A. M., et al. 2017, *AJ*, 154, 86
- Westfall, K. B., Cappellari, M., Bershady, M. A., et al. 2019, *arXiv e-prints* [arXiv:1901.00856]
- Whitmore, B. C., Chandar, R., Kim, H., et al. 2011, *ApJ*, 729, 78
- Wylezalek, D., Zakamska, N. L., Greene, J. E., et al. 2018, *MNRAS*, 474, 1499
- Yan, R., Bundy, K., Law, D. R., et al. 2016, *AJ*, 152, 197
- Yates, R. M., Schady, P., Chen, T.-W., Schweyer, T., & Wiseman, P. 2019, *arXiv e-prints*, arXiv:1901.02890
- Zahid, H. J., Yates, R. M., Kewley, L. J., & Kudritzki, R. P. 2013, *ApJ*, 763, 92
- Zhang, K., Yan, R., Bundy, K., et al. 2017, *MNRAS*, 466, 3217
- Zinchenko, I. A., Pilyugin, L. S., Grebel, E. K., Sánchez, S. F., & Vílchez, J. M. 2016, *MNRAS*, 462, 2715

Appendix A: Comparison with Pipe3D

Pipe3D code (Sánchez et al. 2016, 2018) provides a valid point of comparison to the DAP, since it performs an independent continuum subtraction and emission-line measurements. An overview of the data products released by these two pipelines is provided by Aguado et al. (2019). The output of Pipe3D code on MaNGA data is presented in the MaNGA Pipe3D value-added catalog (VAC)⁴. The MaNGA VAC generated by the Pipe3D team uses MIUSCAT templates for spectral fitting, instead of the MILES models used by the DAP as reported in Sec. 2.2. Specifically, MIUSCAT is a set of simple stellar-population (SSP) models generated according to Vazdekis et al. (2012), that extend the wavelength range of MILES models to cover the range 3465 – 9469 Å. The Pipe3D VAC therefore contains line fluxes for [S III]λ9069. Intriguingly, the publicly-available VAC also contains line fluxes for the [S III]λ9532, which lies outside the MIUSCAT wavelength coverage. It appears that Pipe3D in this case performs an extrapolation of the model continuum for ~ 100 Å (S. Sanchez, private communication).

Fig. A.1 shows the comparison between the emission line fluxes taken into account in this work (y-axis) with the ones obtained with Pipe3D (x-axis) (see also Appendix A, Belfiore et al. 2019) for all the star forming spaxels characterised by a signal-to-noise $S/N(H\alpha) > 15$. In general there is good agreement between the two pipelines, since the majority of the measurements lie in the vicinity of the red dashed line one-to-one line. However, there is a larger spread in the comparison of the [S III] lines with respect to the other transitions, especially for [S III]λ9532. Overall, our [S III]λ9532 measurements are slightly larger than those performed by Pipe3D, while in few cases Pipe3D measurements have values up to two orders of magnitude higher than the ones derived by us. There is good agreement for the [S III]λ9069 emission line, instead. In contrast to Pipe3D, in our fitting procedure we fixed the flux ratio of the two [S III] lines to the intrinsic value of 2.47 (Luridiana et al. 2015), as explained in Sec 2.2. Therefore, the fact that there is good agreement for the [S III]λ9069 but not for the [S III]λ9532 suggests that Pipe3D is underestimating the [S III]λ9532 line flux in the majority of the spaxels, on top of showing a high failure rate of spaxels with clearly nonphysically [S III] line ratios. We therefore strongly recommend against the use of the Pipe3D [S III]λ9532 line fluxes.

Appendix B: Signal-to-noise radial profiles

Fig. B.1 shows the S/N radial gradients of $H\alpha$, $H\beta$, [N II]λ6584, [O II], [O III]λ5007, [S II]λ6717, [S II]λ6731 and [S III]λ9532. To compute these gradient we considered all the spaxels in our galaxy sample, subdivided in bins of stellar mass, as reported in the legend. The radial distance is normalised to the elliptical Petrosian effective radius (R_e), like for all other gradients presented in this work. For each stellar mass bin, the radial profile is computed as the median of the galaxies contributing to the bin at that radius. The upper and lower error bars are obtained by calculating the 16th and 84th percentiles of the distribution for the sample and dividing by \sqrt{N} , where N is the number of profiles at each radius. The figure highlights that the MaNGA galaxy sample used in this work shows sufficient S/N in all the strong lines considered, except for [S III]λ9532 at large radii and for high-mass galaxies.

⁴ <https://www.sdss.org/dr15/manga/manga-data/manga-pipe3d-value-added-catalog/>

Appendix C: Quality test

In order to show the reliability of our method in Fig. C.1 we show the distribution of the difference between the logarithm of the observed value of the emission line fluxes ($H\alpha$, [N II]λ6584, [O II], [O III]λ5007, [S II]λ6717 and [S II]λ6731) and that of the best-fitting model (both normalised to $H\beta$) obtained with IZI, taking into account D13 models and a Gaussian prior on the ionisation parameter (See Sec. 3.4), for all the spaxels used in this work, as a function of radius and stellar mass. The radial distributions are divided in eight bins of stellar mass, in the range $\log(M_\star/M_\odot) = 9 - 11$ in bins of 0.25 dex, as reported in the legend. The shaded areas represent the 16th and 84th percentiles of the distribution in each stellar mass bin divided by \sqrt{N} , where N is the number of galaxies lying in each bin. For each mass bin, a profile is computed only if more than 100 galaxies have a valid measured radial profile. Specifically, the $H\alpha$ and [O III]λ5007 line fluxes are faithfully reproduced at all radii and stellar masses. However, IZI tends to overpredict the [N II]λ6584 and [O II] line fluxes at low stellar masses and to underestimate the [N II]λ6584 at high stellar masses, and the [S II]λ6717 and [S II]λ6731 line fluxes at low stellar masses. Interestingly, concerning the [S II] lines there is a dependence also on radius, since in the most massive galaxies the observed [S II] fluxes are slightly overestimated at radii $R < 1 R_e$, while they are slightly underestimated at radii $R > 1.5 R_e$. Overall, we claim that these stellar-mass- and radius-dependent discrepancies are not affecting the results shown in this paper, because all the radial distributions shown in Fig. C.1 lie in the range [-0.1,0.1] dex, meaning that they are all consistent within the assumed uncertainty of the photoionisation models of 0.1 dex (0.01 dex for $H\alpha$).

Fig. C.2 instead shows the distribution of the difference between the logarithm of the observed flux of the [S III]λ9532 and that of the best-fit model (both normalised to $H\beta$) predicted by IZI, taking into account D13 models and a Gaussian prior on the ionisation parameter, for all the spaxels used in this work, as a function of radius and stellar mass, analogously to Fig. C.1. Unlike the other emission lines, [S III]λ9532 is largely overestimated, with differences between observed and predicted fluxes up to 0.8 dex. Similarly to [S II] lines, there is a dependence also on radius, since in the inner regions ($R < 1 R_e$) of the most massive galaxies the observed [S III] fluxes are overestimated of 0.3 dex more with respect to the values in the outer regions ($R > 1 R_e$).

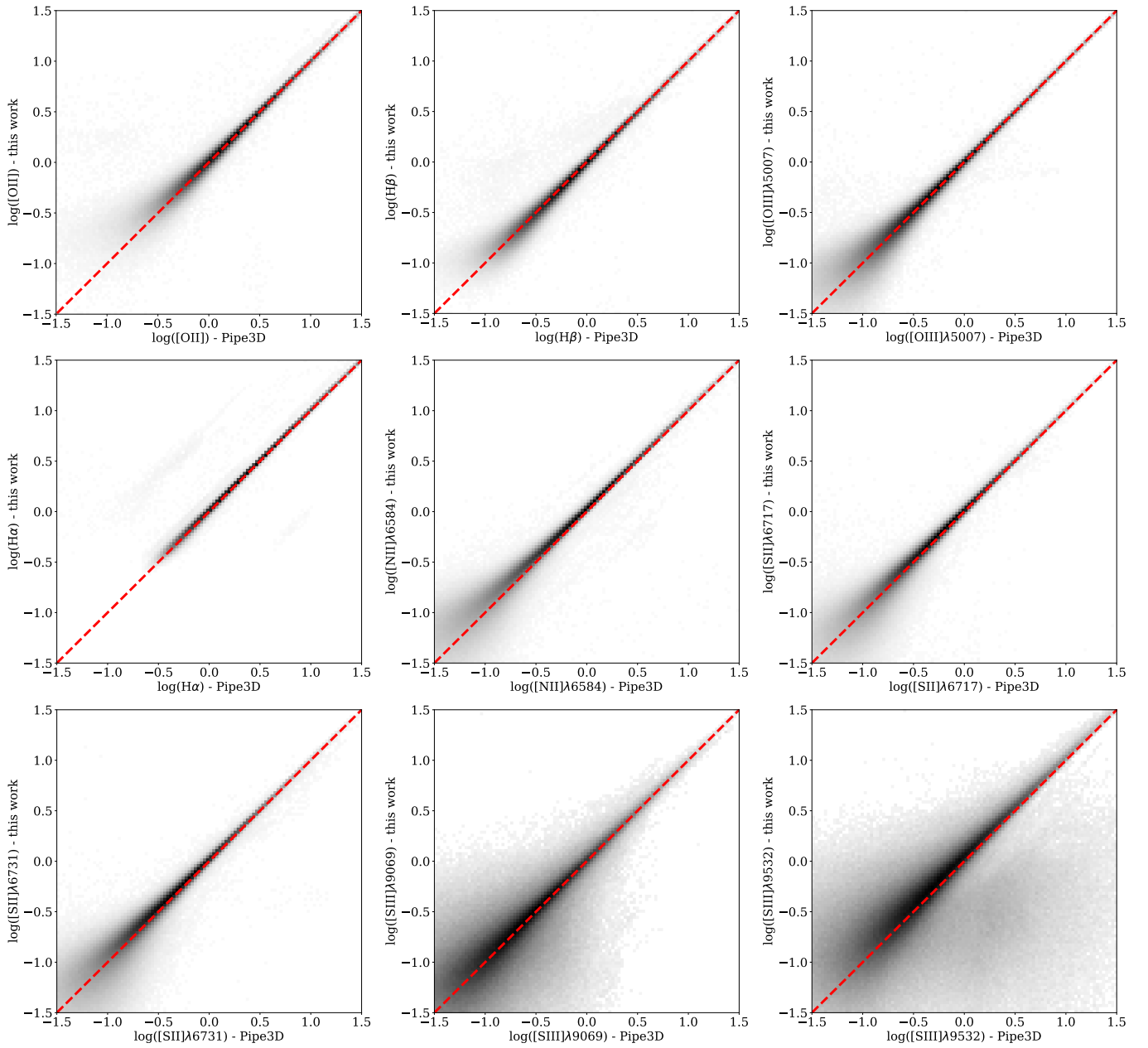


Fig. A.1. Spaxel-by-spaxel comparison between the emission line fluxes taken into account in this work (y-axis) and the results of Pipe3D (x-axis): namely [O III] λ 5007, H β , [O III] λ 5007, H α , [N II] λ 6584, [S II] λ 6717, [S II] λ 6731, [S III] λ 9069, [S III] λ 9532. The fluxes are in units of 10^{-17} erg s $^{-1}$ Å $^{-1}$ cm $^{-2}$ and are expressed in logarithm. The red dashed line represents the one-to-one line.

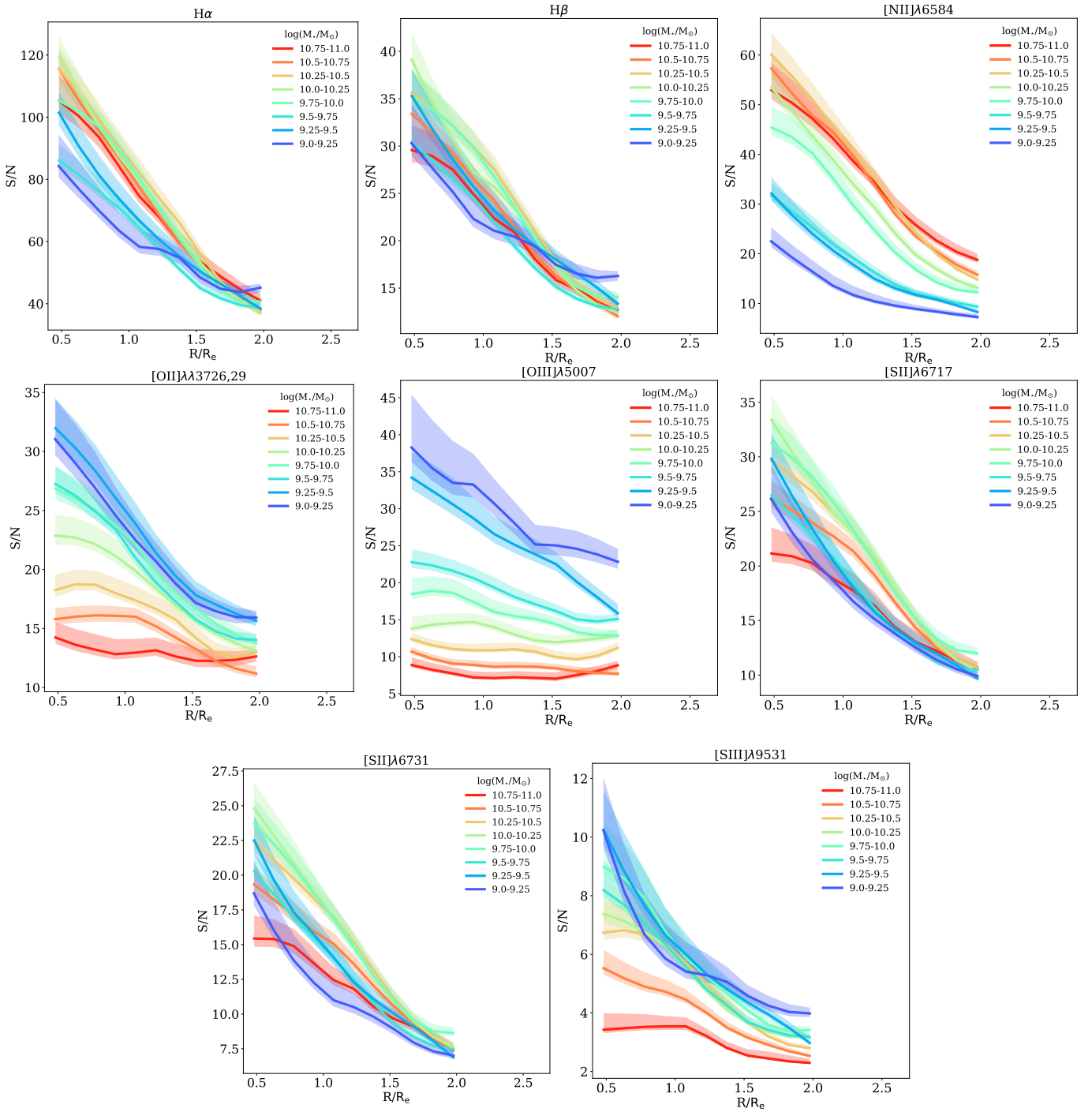


Fig. B.1. Radial distribution of the signal to noise of $H\alpha$, $H\beta$, $[N\text{II}]\lambda 6584$, $[O\text{II}]\lambda 3726,29$, $[O\text{III}]\lambda 5007$, $[S\text{II}]\lambda 6717$, $[S\text{II}]\lambda 6731$ and $[S\text{III}]\lambda 9532$, in eight stellar mass M_\star bins, as reported in the legend.

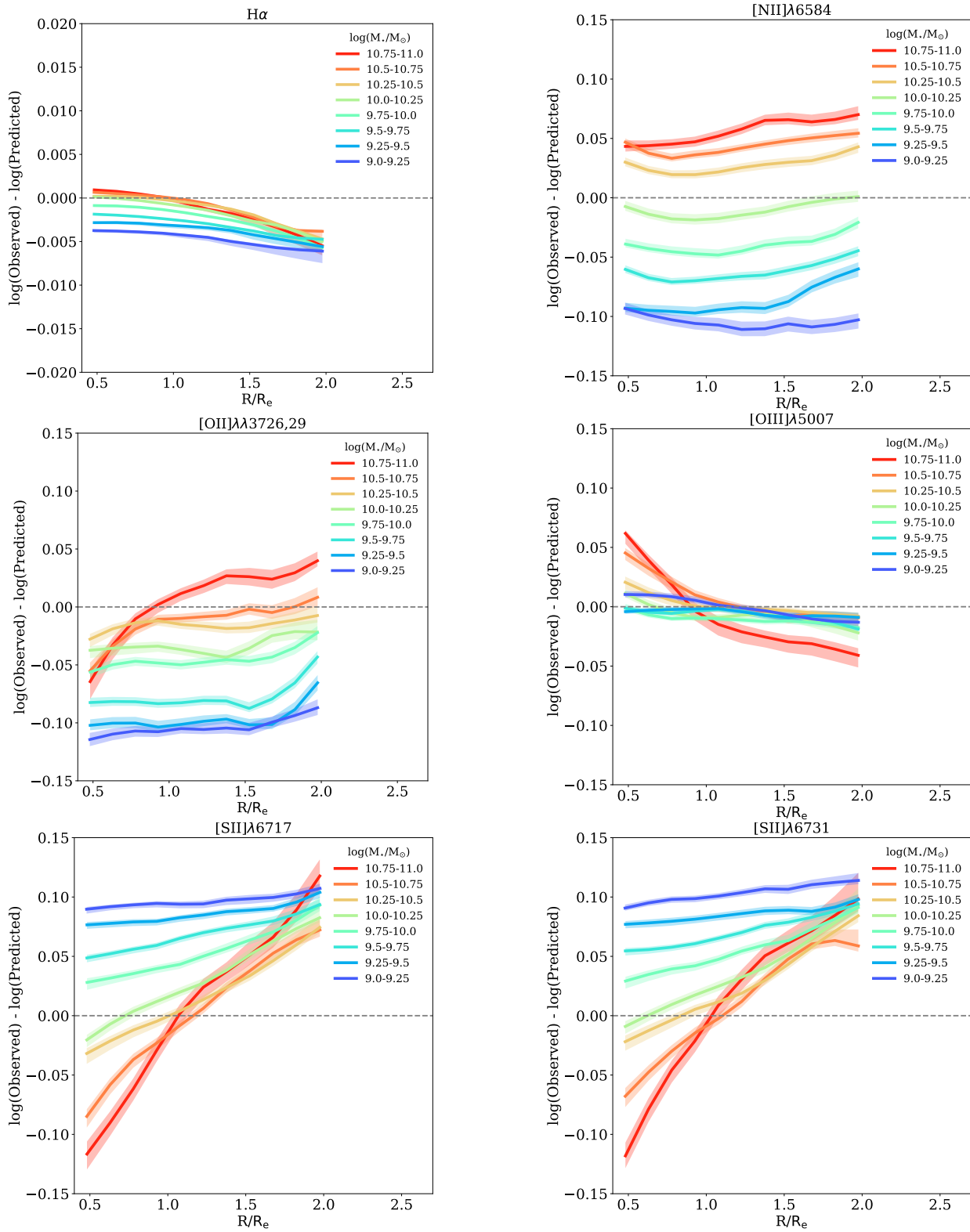


Fig. C.1. Radial distribution of the difference between the logarithm of the observed flux and that of the best-fit model (both normalised to $H\beta$) obtained with IZI and a Gaussian prior on the ionisation parameter, for all the emission lines taken into account, in eight stellar mass M_\star bins, as reported in the legend. Since these radial distributions lie in the range $[-0.1, 0.1]$ dex, it means that they are all consistent within the intrinsic error taken into account for the models.

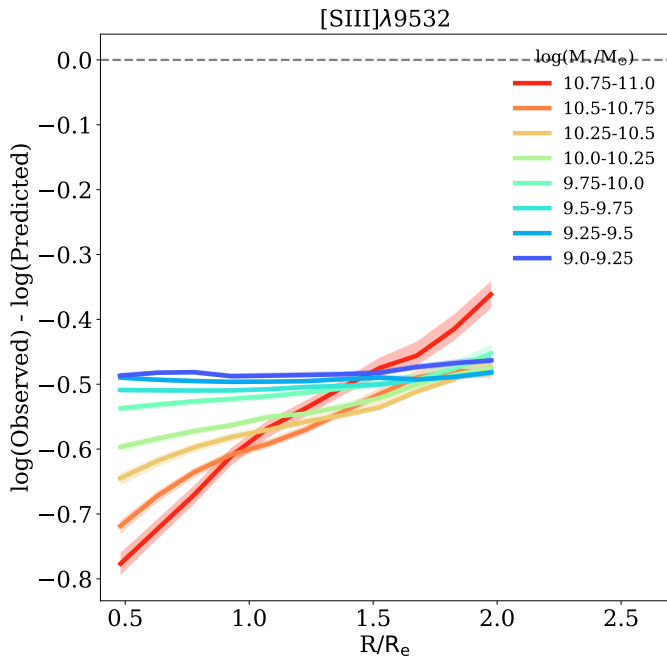


Fig. C.2. Radial distribution of the difference between the logarithm of the observed $[\text{S III}]\lambda 9532$ flux and that of the best-fit model (both normalised to $H\beta$) predicted by IZI, in eight stellar mass M_* bins, as reported in the legend. This clearly shows that $[\text{S III}]\lambda 9532$ is largely overestimated, with differences between observed and predicted fluxes up to 0.8 dex.